Chapter 6

Liquid Mixing in Bubble Columns

In this chapter a new model for liquid mixing in bubble columns is developed based on a fundamental description of liquid mixing as dictated by fluid dynamics in the column. The main motivation behind deriving and solving such a model is the availability of experimental data for the necessary input fluid dynamic parameters from CARPT and CT. Such experimental data enables the solution of the model equations without having to resort to solving the momentum balance equations for calculating the phase distribution and velocity field. The experimental data from CARPT and CT are based on long time averaged measurements that result in steady time averaged velocity and holdup profiles. The instantaneous random motion of the liquid induced by bubbles is accounted for by the turbulent eddy diffusivities. Such a model characterizes, in a statistical sense, the large (marco and meso-scale) scale flow pattern and mixing in the column, which should prove useful for the design of bubble column reactors.

It is noted that, since long time averaging is used to arrive at the model equations, the present model therefore only describes the meso and macro scale mixing in the column. Micromixing phenomena are not captured, but this is not a serious drawback since most of the reactions in bubble columns are slow to moderately fast where the characteristic reaction time is larger than the micromixing time scale.

The derivation of the model equations for a two dimensional axisymmetric flow field, is presented in the following section. The ability of the model to match experimental observations is then illustrated for two cases. The first case is an air-water laboratory scale bubble column, for which the fluid dynamic parameters are directly measured using CARPT and CT. In the second case, the model is applied to characterize liquid (slurry) mixing in an industrial slurry bubble column reactor under reaction conditions. Since experimental measurements of the fluid dynamic input parameters to the model are not available under such conditions, the scale-up rules developed in Chapter 5 are used to evaluate the model parameters in the industrial unit.

6.1 Two Dimensional Convection-Diffusion Model for Liquid Mixing in Bubble Columns

The fundamental two-fluid model mass balance equation for the local, instantaneous tracer species for phase k, is given by the following equation:

$$\frac{\partial \rho_k C_k}{\partial t} + \nabla . \rho_k C_k \vec{u}_k - D_m \nabla^2 C_k = 0 \tag{6.1}$$

with an interfacial jump condition for mass transfer across the interface:

$$\sum_{k=1}^{2} \rho_k C_k [\vec{u}_k - \vec{u}_{ki}] . \vec{n}_k = 0 \tag{6.2}$$

In the above equation, the phase density, ρ_k, for incompressible flows such as in bubble columns, can be considered to be constant. D_m is the molecular diffusivity, which is small and will be neglected hereafter. Phasic or ensemble averaging of the above

equation in an axisymmetric system, for an inert, non-volatile tracer, yields:

$$\begin{aligned}
&\frac{\partial}{\partial t}(\rho_k \epsilon_k \langle C_k \rangle^x) + \frac{\partial}{\partial z}\rho_k(\epsilon_k \langle u_{z,k} \rangle^x \langle C_k \rangle^x \quad + \quad \epsilon_k \langle u'_{z,k} C'_k \rangle^x) + \\
&\frac{1}{r}\frac{\partial}{\partial r} r \rho_k(\epsilon_k \langle u_{r,k} \rangle^x \langle C_k \rangle^x + \epsilon_k \langle u'_{r,k} C'_k \rangle^x) \quad = \\
&\qquad\qquad\qquad\qquad\qquad\qquad\qquad\qquad \langle \rho_k C_k (\vec{u}_k - \vec{u}_{ki}).\nabla X_k \rangle \qquad (6.3)
\end{aligned}$$

where $\langle\ \rangle^x$ represents phasic averaging, as discussed in Chapter 2.3. The right hand side of Equation 6.3 represents the term due to mass transfer across the interface, where X_k is the phase function, defined in Chapter 2.2. An additional source term to represent reaction, can be added to the right hand side of the equation. For the present situation, considering a non-volatile inert liquid tracer, the right hand side of Equation 6.3 is set to 0. Since the model is primarily concerned with the liquid phase, the subscript $k = l$, denoting the liquid phase, is dropped. In addition, all symbols denoting averaging are also dropped, in order to simplify notation. All the variables representing the fluid dynamic parameters and the tracer concentration will denote the phase averaged quantities.

The cross-correlation terms between the fluctuating velocity and tracer concentration are closed using a standard gradient diffusion model (Hinze 1975; Tennekes and Lumley 1971; Seinfeld 1986), as

$$\langle u'_z C' \rangle^x = -D_{zr}\frac{\partial C}{\partial r} - D_{zz}\frac{\partial C}{\partial z} \qquad (6.4)$$

and

$$\langle u'_r C' \rangle^x = -D_{rr}\frac{\partial C}{\partial r} - D_{rz}\frac{\partial C}{\partial z} \qquad (6.5)$$

but, CARPT experiments show that

$$D_{zr} = D_{rz} \sim 0 \qquad (6.6)$$

Therefore

$$\langle u_z' C' \rangle^x = -D_{zz} \frac{\partial C}{\partial z} \tag{6.7}$$

$$\langle u_r' C' \rangle^x = -D_{rr} \frac{\partial C}{\partial r} \tag{6.8}$$

where D_{zz} and D_{rr} are the CARPT measured axial and radial turbulent eddy diffusivities, respectively. Therefore, the final form of the model equation is:

$$\frac{\partial(\epsilon C)}{\partial t} + \frac{\partial}{\partial z}(\epsilon u_z C) + \frac{1}{r}\frac{\partial}{\partial r}(r \epsilon u_r C) = \frac{1}{r}\frac{\partial}{\partial r}[r \epsilon D_{rr} \frac{\partial C}{\partial r}] + \frac{\partial}{\partial z}[\epsilon D_{zz} \frac{\partial C}{\partial z}] \tag{6.9}$$

Standard boundary conditions are used with zero flux at the wall and at the centerline of the column. For the case with continuous flow of liquid through the column, a zero gradient is assumed at the outlet with injection of tracer at the inlet. Equation 6.9 represents the averaged balance equation for the non-volatile liquid species, and is a transient two dimensional convection-diffusion equation. The phasic (or time) averaging that has been performed (Equation 2.23) to arrive at this equation refers to any time interval, which may be small or large.

Multiphase flows in bubble columns are highly transient in nature. Hence the length of the time interval considered in the averaging will affect the type of results obtained. Short time averages involve averaging which is done over a small time interval, large enough to smooth the variations across the interface but small enough to capture some of the transient structures in the flow. With this averaging some of the transient structures in the flow can be captured. These transient structures will vary in nature with the time interval of averaging. On the other hand, long time averaging results in a statistically stationary flow field, which is steady in time, in terms of all the fluid dynamic variables.

Two factors are of concern here in deciding the type of averaging to be considered for the above model equation. First, since the flow phenomena in bubble columns

is highly turbulent and random in nature, a quantitative comparison of the fluid dynamic parameters, between model predictions and experimental measurements, can only be made with respect to the statistical properties of the flow field. This immediately implies that time or ensemble averaging is required. Second, since the present model is considered in a two-dimensional axisymmetric domain, the type of boundary conditions used (zero gradient at the centerline) will not permit the computation of physically realistic results describing the transient structures. A true transient behavior can only be represented in a fully three dimensional flow model which can capture the inherent vortical and spiraling motion of the flow in bubble columns.

For these reasons, it is proposed to consider long time averaging for the above model equation. The various averaged quantities in the above equation will hence refer to long time averaged quantities and corresponding closure models (Equations 6.7 and 6.8). CARPT data for the long time averaged liquid velocities, u_r and u_z, and turbulent diffusivities, D_{rr} and D_{zz}, along with CT data for the time averaged liquid holdup profile, are used as input parameters to the model.

6.1.1 Numerical Procedure for Solution of Model Equations

A finite volume (also referred to as the control volume) method has been used to solve the convection-diffusion model (Patankar 1983). In this scheme, the calculation domain is divided into a number of non-overlapping control volumes, such that there is a control volume surrounding each grid point. The governing equations are integrated over each volume, with piecewise profiles for the variation of the dependent variables. This results in the discretization equation containing the values of the dependent variables for a group of grid points. The discretization equation obtained as such allows the conservation principle for a given quantity to be expressed for the finite control volume. The most attractive aspect of this method is that the resulting solution guarantees that the integral conservation of a given quantity is exactly satisfied over a single or group of control volumes, and therefore over the whole domain. Thus, even the coarse-grid solution exhibits exact integral balances.

Discretization considerations

An implicit scheme is used in time, with upwinding for the convection term. Although the upwind scheme is only first order accurate, it has been shown to have advantages in solving nonlinear systems with steep velocity gradients (Patankar 1980) as in the case of bubble column flows. However, if the physical diffusion process is dominant (i.e. if D_{zz} and D_{rr} are very large), upwind differencing loses its advantages and requires finer discretization. A staggered grid configuration is used, by assigning the scalar variables, namely the concentration and holdup to the cell center and the vector velocity variables and diffusivities to the cell faces (Figure 6.1). Advantages of using the staggered grid configuration, for solution of the momentum balance equations, have been discussed elaborately by Verstaag et al. (1995) and Patankar (1983). For solution of the convection-diffusion equation it poses no special advantage.

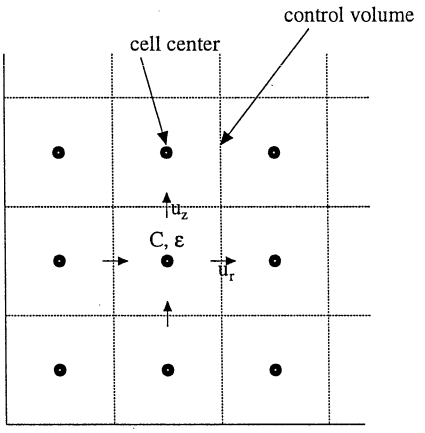

Figure 6.1: Variable Locations in a Staggered Grid

The above process of discretization results in a set of linear algebraic equations. Since the model equation is a transient convection-diffusion equation, this results in a sparse matrix. Therefore a direct method is used to solve the system of equations, based on LU decomposition. The model is two dimensional, resulting in extremely large number of equations which depend on the size of the domain studied. The

SMPAK^{TM} solver, which uses an effective storage scheme to hold large sparse matrices, is used to solve the equations. This significantly reduces the memory and time (five times lower than a standard solver) for computation. The spacing used in the three coordinates, Δ t, Δ z and Δ r, are the numerical parameters that need to be considered. Although stability is not a concern since an implicit scheme is used, the issue of accuracy should be examined. For this purpose, several trials are made with increasingly fine discretizations, until an accurate solution is obtained.

There is considerable experimental evidence in the literature, including results from CARPT (Chapter 4), which show that in columns of high aspect ratios the time averaged flow pattern is axisymmetric with global liquid recirculation in the column. In a time averaged sense, a large scale liquid circulation exists in the form of a recirculation cell, which occupies most of the column, with respect to height, with liquid ascending along the central core region and descending along the annular region between the core and the walls. A single one dimensional velocity profile is always identified in this recirculation cell, which is in the middle part of the column. Axial variations are evident in the distributor and free surface region, where the liquid turns around. In the middle region, there is evidence that all the other fluid dynamic parameters, such as the turbulent eddy diffusivities and the turbulent stresses are also a function of radial position only.

The computation domain is therefore divided axially into three regions: a distributor zone at the bottom, a fully developed region where the radial liquid velocities are negligible and are considered to be zero, and finally the disengagement zone at the top where liquid turns around. The distributor and disengagement zones are assumed to extend over a height equal to one column diameter, based on experimental considerations. However, varying the height from 1 to 2 times the column diameter does not affect the results significantly (Figure 6.6), especially for column aspect ratios greater than 10. In the distributor zone and the disengagement zone, the domain is discretized only in the radial direction, as shown in Figure 6.2. In both these regions where the radial liquid velocities are significant, it is found that

the solution of the equations becomes very sensitive to the radial velocities. The velocities assigned to these regions are therefore fitted to a smooth profile in order to satisfy liquid continuity for each control volume or cell, and therefore the entire domain. In the fully developed middle region, the domain is discretized both radially and axially (Figure 6.2), and the radial liquid velocities are set to zero. The other

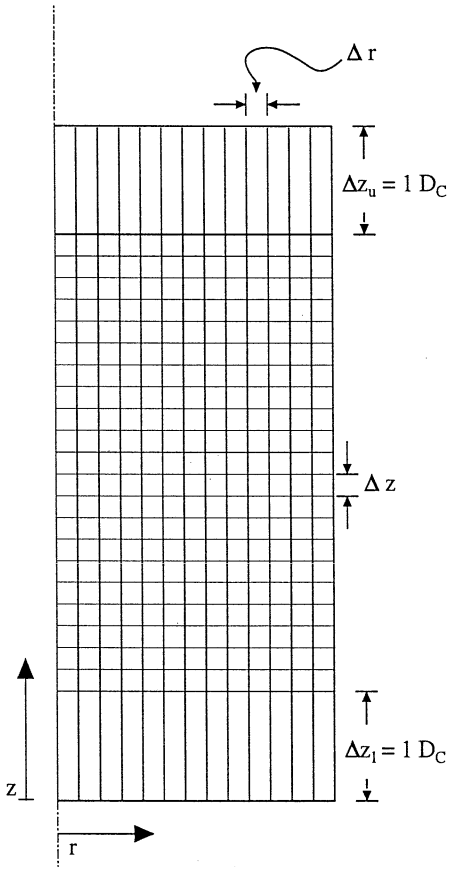

Figure 6.2: Schematic of Column Discretization

fluid dynamic variables, i.e., the axial liquid velocity, axial and radial turbulent eddy diffusivities are considered to be a function of radial position only and independent of axial location in the middle section of the column. Experimental data from CT for the liquid holdup, is first fitted to the power law expression given by Equation 2.7 to obtain the radial liquid holdup profile, which is then used as an input to the one dimensional liquid recirculation model (Appendix A) to obtain an axial liquid velocity profile that fits the experimental data from CARPT measurements under the

same operating conditions. These radial profiles for the liquid holdup and velocity are used as input to the model in the middle fully developed section of the column, along with radial profiles for the axial and radial turbulent eddy diffusivities. Using these calculated profiles for the holdup and velocity ensures continuity to be satisfied in the entire domain. The developed model is used to simulate tracer responses for different cases for which experimental data is available.

6.1.2 Case I: Air-Water System

The model is first tested in a column under operating conditions for which experimental data for the fluid dynamic parameters are directly available. The case considered is the tracer data of Myers et al. (1986), whose experiments were conducted in an air-water system in a column of diameter 19 cm, at a superficial gas velocity of 10 cm/s and liquid velocity of 1 cm/s. The mode of operation, in this case, is therefore a cocurrent bubble column with a continuous flow of liquid and gas. The appropriate boundary conditions for the model are:

$$r = 0, \quad r = R; \qquad \frac{\partial C}{\partial r} = 0 \tag{6.10}$$

$$C(r, 0, t) = \delta(t) \tag{6.11}$$

$$z = L, \qquad D_{zz}(r) = 0; \quad \frac{\partial C}{\partial z} = 0 \tag{6.12}$$

A time step of 0.5 sec along with a radial grid size of 0.38 cm and an axial grid size of 1 cm were found to be optimum discretizations. In the end zones, the cell heights are assigned to be equal to the column diameter. In order to solve the model for the present case, CARPT and CT experiments were performed under identical conditions to obtain the input hydrodynamic parameters for the system. Results are shown in

Figures 6.3, 6.4 and 6.5, for the one dimensional time averaged axial liquid velocity, liquid holdup profile and turbulent eddy diffusivities, respectively.

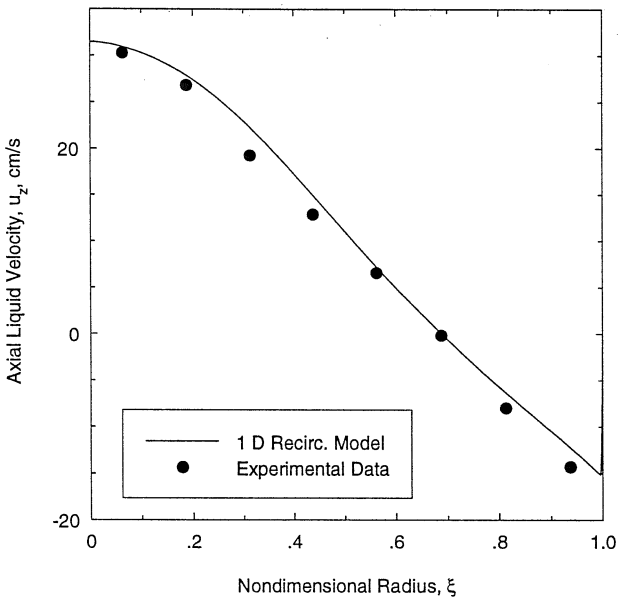

Figure 6.3: Time Averaged One Dimensional Axial Liquid Velocity Profile: Column Diameter 19 cm, $U_g = 10$ cm/s

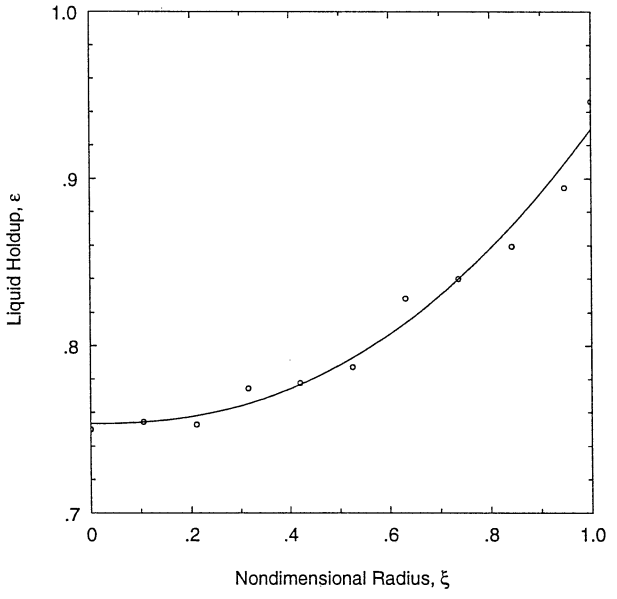

Figure 6.4: Time Averaged Liquid Holdup Profile: Column Diameter 19 cm, $U_g = 10$ cm/s

In Figure 6.3, the solid circles represent the axial liquid velocity axially averaged in the middle section of the column. The curve is the one dimensional recirculation model prediction (Appendix A), using the input holdup profile from CT measurements (shown in Figure 6.4) along with a mixing length profile obtained from CARPT data. With these profiles for the liquid velocity and holdup, continuity is satisfied within 98%. The experimental data for the turbulent diffusivities, in Figure 6.5, are directly used as input to the model.

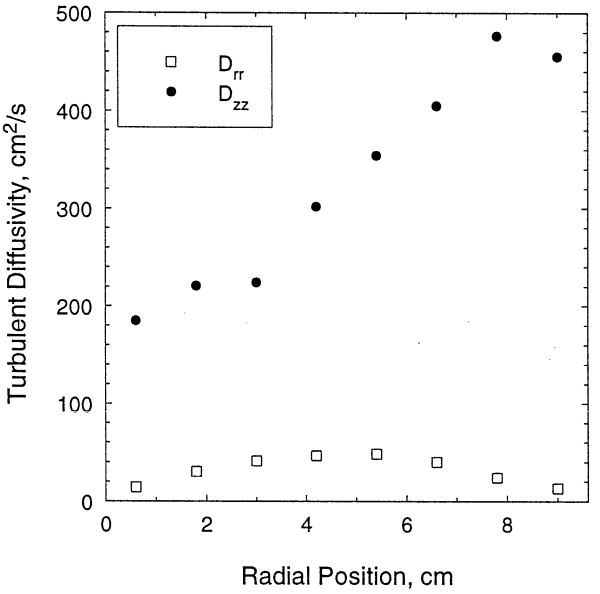

Figure 6.5: One Dimensional Turbulent Eddy Diffusivities: Column Diameter 19 cm, $U_g = 10$ cm/s

Using these results as input, the model is solved to predict the overall tracer impulse response of the given system, shown in Figure 6.6. The comparison between the two dimensional model prediction of the normalized exit mixing cup concentration and the experimental tracer response curve from Myers et al. (1986) (Figure 6.6) suggests that the model provides a good representation of the experimental data. Therefore, a fundamentally based model, with experimental data for the fluid dynamic parameters, is able to capture the overall mixing in the system as described by the tracer residence time distribution (RTD).

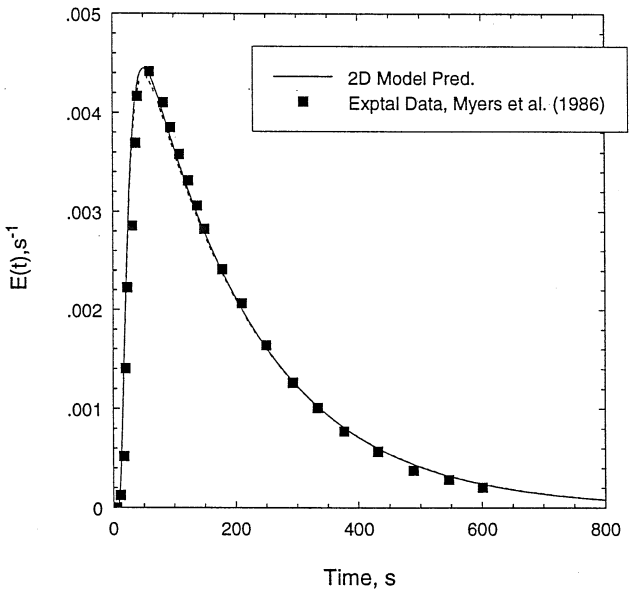

Figure 6.6: Comparison of Experimental Tracer Response with 2D Model Prediction (dashed line is for cell heights, in end zones, equal to two column diameters)

6.1.3 Case II: Interpretation of the AFDU Tracer Data

Experimental Details

Radioactive tracer experiments were conducted by Air Products and Chemicals, Inc. in DOE's Alternate Fuels Development Unit (AFDU), in LaPorte,Texas, which is a slurry bubble column reactor, to study the backmixing characteristics of the gas and liquid phase in this reactor during methanol synthesis. Powdered methanol catalyst ($\sim$ 45 wt % loading) suspended in inert hydrocarbon oil forms the batch slurry phase. Synthesis gas is bubbled through a sparger placed at the bottom of the reactor. The gas disengages from the oil in the freeboard section of the reactor, and the unreacted feed gas is recycled back to the reactor.

The principal reaction for methanol synthesis is

$$CO + 2H_2 \rightleftharpoons CH_3OH \tag{6.13}$$

At the process conditions used, the methanol formed is in the vapor phase. The feed gas to the reactor is synthesis gas which is a mixture typically consisting of

CO (30 %), H_2 (60 %), CO_2 (5 %) and inerts (N_2). The composition of the feed gas may be varied by changing the feed ratio, depending upon process requirements. The presence of CO_2 is usually required, as it serves to initiate the reaction. A side reaction known to occur is the water gas shift reaction:

$$H_2 + CO_2 \rightleftharpoons H_2O + CO \tag{6.14}$$

Based on the above reaction stoichiometry (Equations 6.13 and 6.14), there is a reduction in the volume of the gas due to reaction. The actual reduction depends on the feed rate, composition, and conversion. For the tracer runs studied, feeds with varying composition were used. The experimental conditions along with the feed compositions, observed conversions and changes in gas volumetric flow rate are reported in Table 6.1. The conversion of CO for the three runs studied, ranges from 16% to 33%. An excess of CO results in lower conversion (Runs 14.6 and 14.7 compared to Run 14.8). Although CO conversion varies for the three cases, due to a corresponding change in feed composition, the effective overall change in the gas flow rate is about the same for all the runs, around $-$ 18 %.

Table 6.1: Experimental Conditions (Temp : 250^{0}C)

Run No.	P MPa	Avg. Gas Holdup	Inlet U_{g0} cm/s	Feed Compn. mol %			Conv of CO to MeOH	Inlet Vol. Flow rate SCFH	Change in Flow rate %
				H_2	CO	CO_2			
14.6	5.2	0.39	25	35.4	50.8	12.7	15.9	143121	-17.1
14.7	5.2	0.33	14	35.0	50.9	12.7	17.5	81151	-19.2
14.8	3.6	0.38	36	60.2	24.0	10.3	33.0	141690	-17.7

Gas Holdup Measurements

Holdup measurements within the reactor were made using two techniques: 1. Differential Pressure measurements (DP) and 2. Nuclear Density Gauge (NDG) measurements. Results of the axial gas holdup profiles from each of these measurements are shown in Figure 6.7.

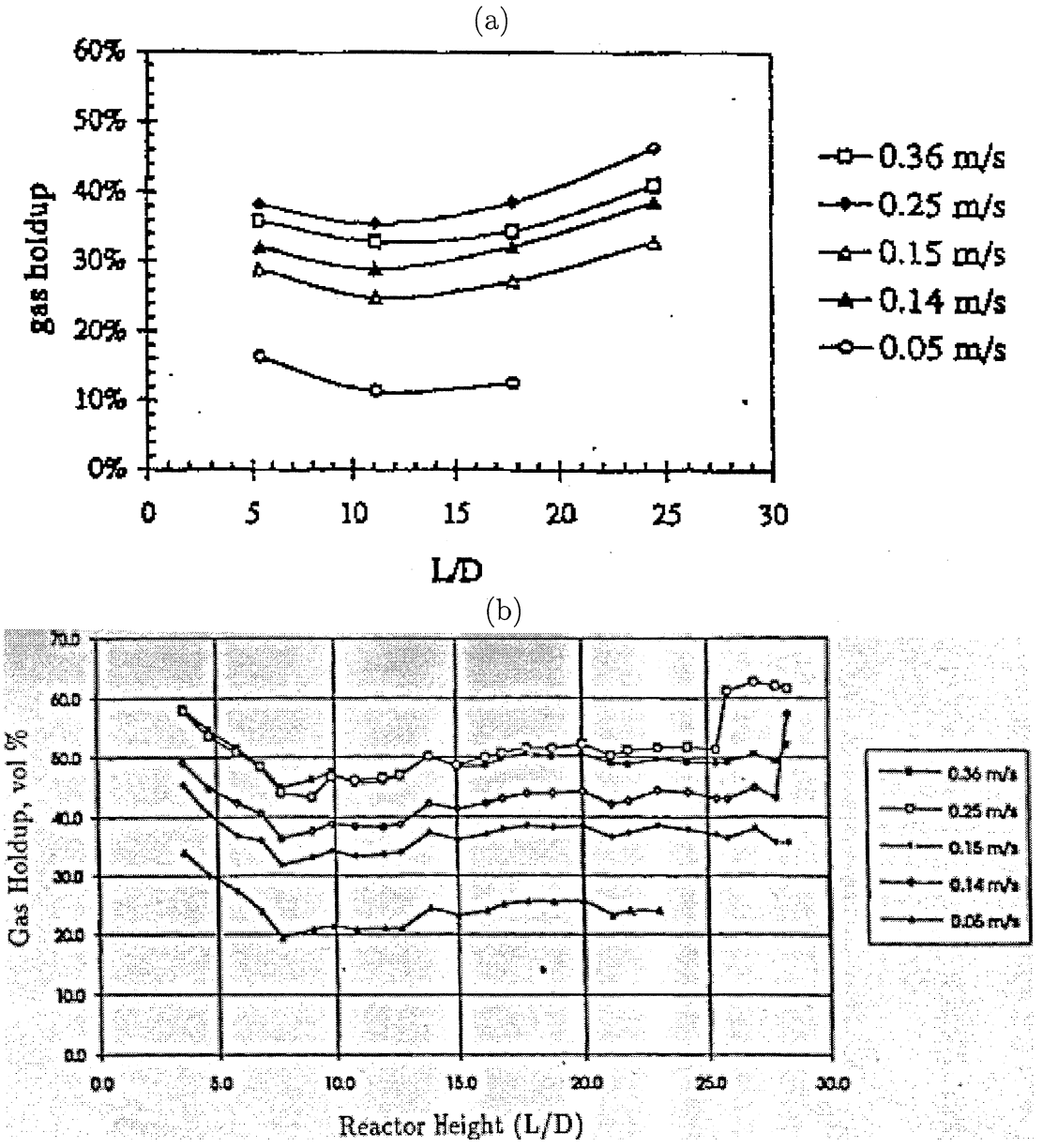

Figure 6.7: Experimentally Measured Axial Gas Holdup Profiles in AFDU During Methanol Synthesis: (a) DP (b) NDG

DP measurements rely on the assumption that liquid (slurry) velocities and shear stresses near the wall are small in comparison with the hydrostatic head. Thereby

$$\rho g = \frac{\Delta P}{\Delta z} \tag{6.15}$$

where

$$\rho = \rho_l \epsilon_l + \rho_g \epsilon_g \tag{6.16}$$

The subscripts 'l' and 'g' refer to the slurry and gas phase respectively. Based on experimental evidence the slurry density in the column is assumed to be uniform (ρ_l) and is calculated using the information on solids holdup ((catalyst weight/density) / dispersion volume) (Shollenberger 1995b). Therefore, from here on the terms 'liquid' and 'slurry' are used interchangeably. The density of the gas phase is very small when compared with that of the slurry, and hence the second term in Equation 6.16 is usually neglected. Equation 6.16 in conjunction with Equation 6.15 can be used to calculate the average holdup between the two measurement sections (Figure 6.8). Assuming that there is no axial variation of holdup between the measurement sections, the volume average holdup calculated from DP measurements yields a cross-sectional mean holdup, $\bar{\epsilon}_g$:

$$\bar{\epsilon}_g = 2 \int_0^1 \xi \epsilon_g(\xi) d\xi \tag{6.17}$$

Nuclear Densitometry (NDG) is a noninvasive method in which a narrow beam of radiation (γ ray) emitted through the center of the column, with the source on one side (Figure 6.8), is detected using a detector on the opposite side. Such a single chordal measurement obtained across the centerline (i.e. diameter) of the column results in a chordal average, $\hat{\epsilon}_g$, defined by

$$\hat{\epsilon}_g = \int_0^1 \epsilon_g(\xi) d\xi \tag{6.18}$$

which is not representative of the cross-sectional mean.

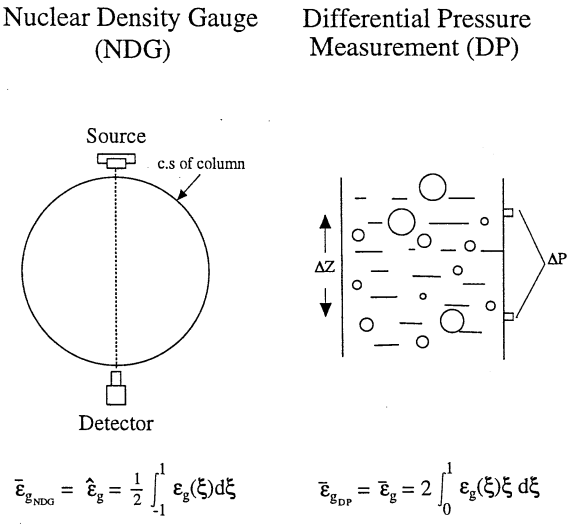

Figure 6.8: Schematic of DP and NDG Technique for the Measurement of the Average Gas Holdup

Therefore there is a discrepancy between the average holdups measured by DP and NDG (Figure 6.7). Using Equation 2.7 for the radial gas holdup profile, given by:

$$\epsilon_g(\xi) = \tilde{\epsilon}_g \frac{m+2}{m}(1 - c\xi^m)$$

the two averages $\bar{\epsilon}_g$ and $\hat{\epsilon}_g$ are found to be related by the following expression:

$$\frac{\hat{\epsilon}_g}{\bar{\epsilon}_g} = \frac{(m+2)(m+1-c)}{(m+1)(m-2c+2)} \tag{6.19}$$

Since experimental measurements of $\hat{\epsilon}_g$ and $\bar{\epsilon}_g$ are available from NDG and DP, the average (axially averaged) of these values is used to extract the void fraction exponent m and c in Equation 2.7, given above, which then provide the description of the radial void fraction profile existing in the column. Using the average gas holdup, $\bar{\epsilon}_g$, in the entire reactor as measured by DP, the resulting void fraction profiles, calculated for all the three process conditions are shown in Figure 6.9.

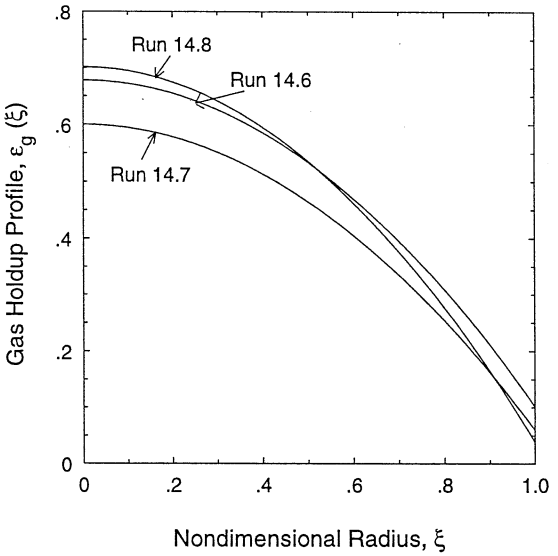

Figure 6.9: Radial Gas holdup Profiles Calculated from Global Gas holdup Measurements (DP and NDG) in the AFDU During Methanol Synthesis

Tracer Experiments

A schematic of the AFDU slurry bubble column reactor is shown in Figure 6.10. It has an internal diameter of 0.46 m and a height of 15.24 m, with the liquid - gas - solid dispersion level maintained at 13.25 m (L/D ratio of 28.8) during the runs discussed here. The vapor phase and liquid phase tracer experiments were conducted separately. Radioactive Ar-41, used to study the residence time distribution of the vapor phase, was injected as a pulse at the inlet of the reactor. Radioactive Manganese-56 (50 μm) particles mixed in oil were used for liquid (slurry) phase tracing. Four pulse injections were made at a given process rate: (1) lower nozzle N2 - 4.5″ (11.4 cm) from wall, (2) nozzle N2 - at wall, (3) upper nozzle N1 - 4.5″ (11.4 cm) from wall, and (4) nozzle N1 - at wall. The axial levels of these injection points are shown in Figure 6.10. The injections made at 4.5″ (11.4 cm) from the wall are referred to as 'center injections', as they are made into the core part of the column where the liquid is known to move upward by convection in the time averaged sense.

Radiation measurements from the vapor and liquid tracers were made using thirty 2″ by 2″ NaI scintillation detectors positioned outside the column, at various

axial levels, as shown in Figure 6.10. Sets of four detectors were placed at 90 degree angles at seven axial locations. In addition, detectors were placed at the inlet and outlet of the reactor. During the liquid tracer study, the inlet detector was placed close to the liquid injection point to monitor the shape of the injected pulse. The

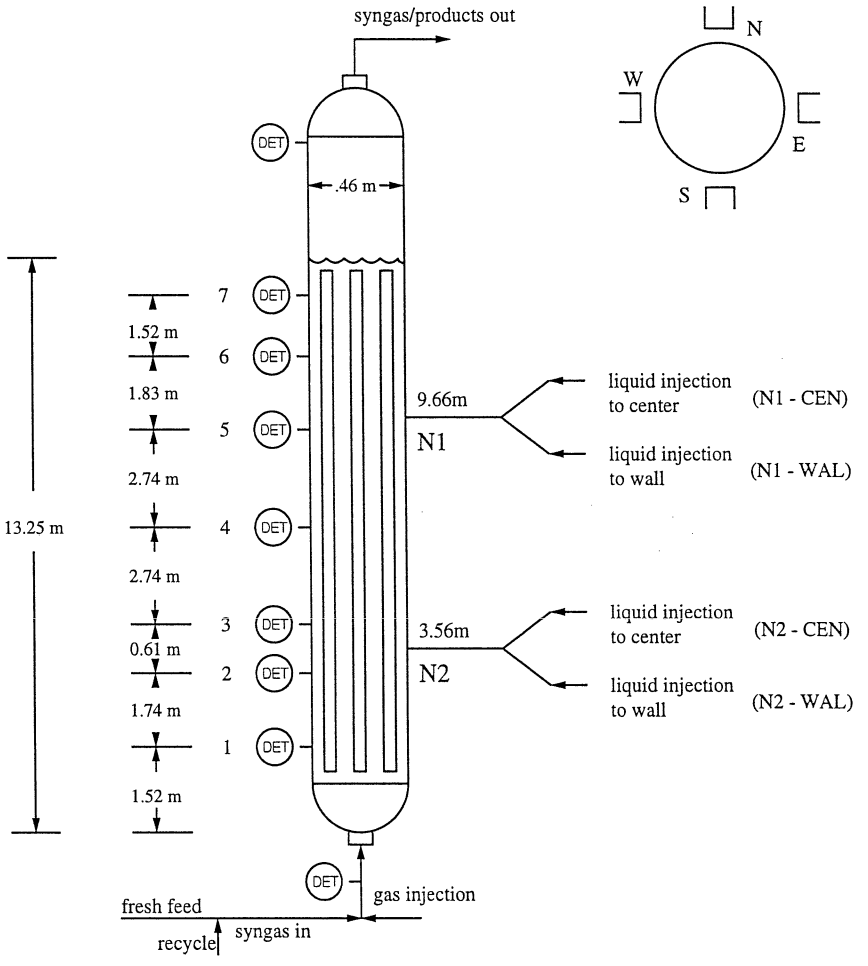

Figure 6.10: Schematic of Reactor for Tracer Experiments

detectors were shielded on their sides thereby allowing only the front circular surface of the detectors to be exposed to radiation. With this configuration, the spatial range from which a detector received most of its radiation is assessed. Details of these calculations are discussed in a quarterly report for DOE (Degaleesan et al. 1996b), and are given in Appendix D. It has been shown that most of the intensity recorded

at a detector, shielded on its sides, comes from a slice of volume at the given axial level of the detector. For analyses purposes only the tracer from the cross-section of the reactor at the axial location of the detector is considered here.

Model Parameters

In order to use the present model to predict liquid tracer distribution in the column it is necessary to evaluate the model parameters. Experimental information exists only for the average gas holdup. As seen in Figure 6.7, there is an axial variation of the gas holdup in the reactor due to reaction. This variation is not very significant as far as the slurry phase mixing is concerned, and as a first approximation, the average gas holdup in the reactor as obtained from DP measurements is considered. The corresponding radial gas holdup profiles calculated using results from DP and NDG are shown in Figure 6.9. Information on the other fluid dynamic variables, namely, the liquid velocity profile and turbulent eddy diffusivities does not exist. Hence the preliminary scale-up rules and characterization methodology, developed in Chapter 5, were used to evaluate the mean liquid recirculating velocity and average turbulent eddy diffusivities. Since the present experimental conditions involve high pressure and a slurry system, this significantly alters the overall gas holdup in the reactor (Wilkinson et al. 1992), which for the present case results in gas holdups higher than that at atmospheric conditions for air-water systems. Knowing the average gas holdup in the reactor (Table 6.1) and using Equation 5.2, the equivalent gas velocity, U_{ge}, for the three operating conditions is calculated (shown in Table 6.3). For Run 14.6, $U_{ge} = 47$ cm/s, which is considerably higher than the original inlet gas velocity of 25 cm/s. The estimated U_{ge} is used in Equations 5.5 to 5.9, to evaluate the mean recirculation velocity and average axial and radial turbulent diffusivities under the existing conditions in the AFDU.

The liquid recirculating velocity profile, $u_z(r)$, is then calculated by the procedure outlined in Figure 5.3 in Chapter 5, using as input the holdup profile estimated

from DP and NDG measurements (Figure 6.9), and the knowledge of the mean recirculation velocity, $\overline{u}_{rec}$. The liquid (slurry) recirculation velocity profile, evaluated in this manner is shown in Figure 6.11, for Run 14.6. The centerline velocity calculated

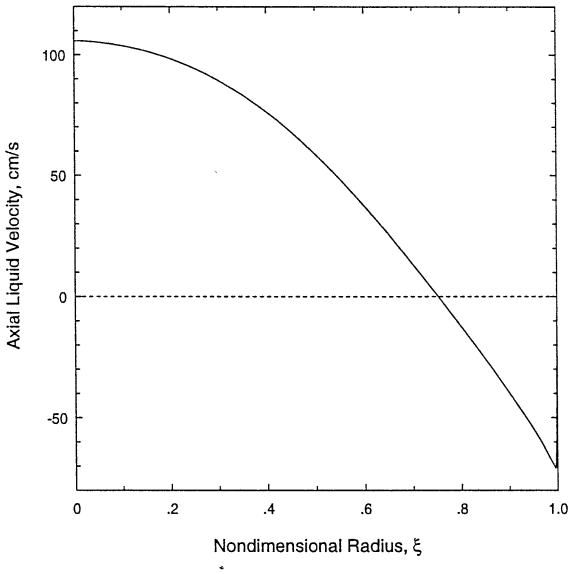

Figure 6.11: Calculated Axial Liquid Velocity Profile for Run 14.6, in the AFDU Reactor During Methanol Synthesis

is in the order of 1 m/s. Due to the large area and higher liquid holdup near the wall, the magnitude of the maximum downward liquid velocity is much lower than the centerline velocity, in order to satisfy mass balance for the liquid (in batch mode). The radial profiles for the axial and radial eddy diffusivity are calculated from Equations 5.10 and 5.12, respectively, along with the estimated average values (Table 6.3). The profiles for the axial and radial eddy diffusivities, calculated in this manner for Run 14.6 are shown in Figures 6.12 and 6.13, respectively.

Heat exchanger tubes are present in the AFDU reactor for cooling the medium. There are 24 one inch (O.D.) tubes, which occupy approximately 7.5 % of the cross-sectional area of the reactor, and extend over the entire length of the dispersion. The effect of the heat exchanger tubes are accounted for only with regard to the radial turbulent eddy diffusivity, since the presence of these tubes will physically reduce the radial length scales of turbulence. Liquid recirculation and the axial eddy diffusivity

are assumed to be affected to a much lesser extent, and for the present calculations these effects are neglected.

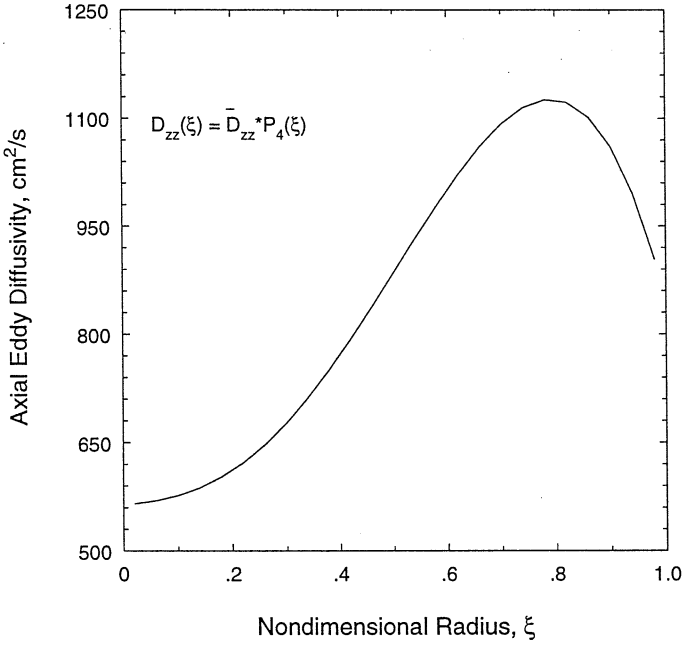

Figure 6.12: Calculated Axial Eddy Diffusivity Profile for Run 14.6, in the AFDU Reactor During Methanol Synthesis

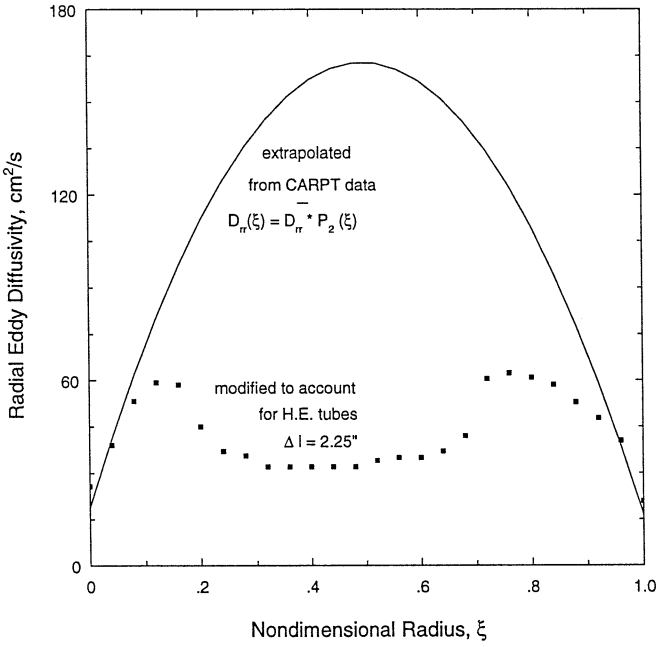

Figure 6.13: Calculated Axial Eddy Diffusivity Profile for Run 14.6, in the AFDU Reactor During Methanol Synthesis

A cross-sectional view of the reactor in the presence of these tubes is shown in Figure 6.14. The tubes are present in two annular rings about the center of axis of the reactor, near the region of flow inversion, and will affect the radial turbulent diffusivities in this region by restricting the radial length scale of turbulence in this region. This is accounted for by considering the characteristic spacing between the

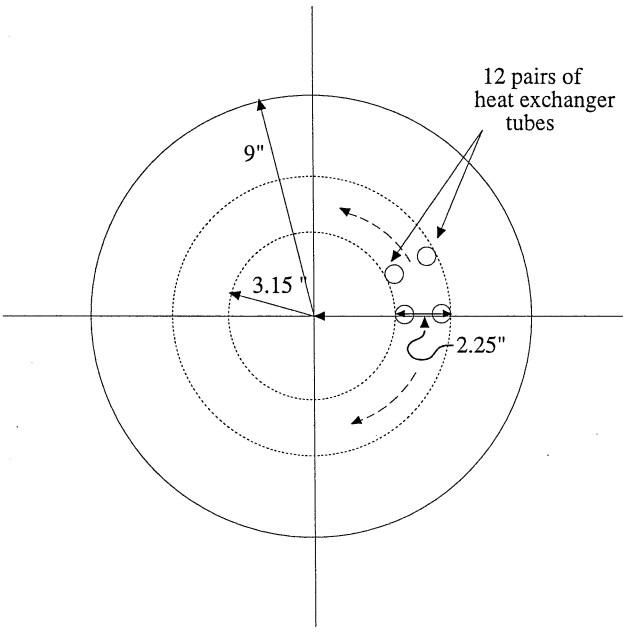

Figure 6.14: Schematic of the Cross-sectional View of the AFDU Reactor showing Placement of Heat Exchanger Tubes

tubes, which is about 2.25″ (5.7 cm), as an effective diameter and estimating the average radial diffusivity for this diameter (5.7 cm). Equation 5.9, which was originally developed for large diameter columns (> 10 cm), is modified by retaining the 0.3 power dependence of D_{rr} on D_c and U_g (Equation 5.9) for smaller column diameters. Considering the CARPT data for the 14 cm diameter column as a reference, the following equation for the radial diffusivity for $D_{c_{eff}} = 5.7$ cm is used:

$$\overline{D}_{rr(D_c=5.7)} = (\frac{5.7}{14.0})^{0.3} \ \overline{D}_{rr(D_c=14)} \tag{6.20}$$

The above equation results in a radial diffusivity of 35 cm^2/s. The estimated value of the radial diffusivity in the region of the tubes, results in a modified profile for the radial eddy diffusivity, denoted by the dashed line in Figure 6.13. This represents a first approximation in accounting for the effect of heat exchanger tubes in the AFDU reactor. Thereby, all the input fluid dynamic parameters to the model are evaluated.

Simulation Results

The initial and boundary conditions are given below. Since the liquid is in batch mode, zero flux conditions are applied at the boundaries:

$$r = 0, \quad r = R; \qquad \frac{\partial C}{\partial r} = 0 \tag{6.21}$$

$$z = 0, \quad z = L; \qquad \frac{\partial C}{\partial z} = 0 \tag{6.22}$$

The initial condition is assigned according to the location of tracer injection during an experiment. In the actual tracer experiment, the injection is made locally at a certain (r_i, θ_i, z_i). However, since the model is two dimensional, for modeling purposes the injection is considered to be made in an annular ring (r_i, z_i). The initial condition is given as: At t=0:

$$\begin{aligned} C(r,z,t) &= f_t(t) \qquad r = r_i, \quad z = z_i \\ &= 0 \qquad r \neq r_i, \quad z \neq z_i \end{aligned} \tag{6.23}$$

$f_t(t)$ describes the pulse of tracer injected (close to an impulse function), and is fitted to the response of the detector close to the location of injection. For a given experimental condition, four tracer experiments were carried out with four different locations of the injection point. These are (r_i and z_i are given in cm) given in Table 6.2.

In order to compare the experimental results with model predictions, the individual detector responses measured by the four detectors at each axial level are averaged to yield an averaged detector response at each detector level. Averaging

Table 6.2: Positions of Tracer Injection in the Model

	r_i (cm)	z_i (cm)
Wall Injection at N1	22.8	966.0
Center Injection at N1	11.5	966.0
Wall Injection at N2	22.8	356.0
Center Injection at N2	11.5	356.0

is done since the present model is only two dimensional, and cannot distinguish any angular variations in tracer concentration. Responses of the individual detectors at two axial levels (shown in Appendix F for Run 14.6) indicate that such an (angular) averaging of the four detector response at a given axial location is a reasonable approximation. The averaged experimental detector responses measured at the seven detector levels, for the wall injection at level N1 in Run 14.6. are shown in Figure 6.15. It is to be noted that the various detector level responses, in Figure 6.15, do not all show equal measurements at large times, which is what is expected if the tracer is eventually uniformly distributed in the reactor. The reason for this is the improper normalization of the detector responses. Specific details and reasons for this are shown in Appendix E, where suggestions have been made to improve the quality of the tracer data. Due to this, the experimental detector responses cannot be quantitatively compared with the model predictions of the tracer distribution in the column. Only the characteristic mixing times as measured by the times of the peaks of the curves can be compared.

The radiation intensity emitted, per unit volume, by the tracer is directly proportional to the tracer concentration. Since the experiments involve radioactive tracer, the measurements, as detected by the scintillation detectors, represent neither local nor average tracer concentration, but the attenuated cumulative tracer concentration in a given cross-sectional plane. The detectors are shielded on their sides. Hence most of the radiation detected, comes from the cross-sectional plane at the axial level of the detector. In order to compare the model predictions with the averaged

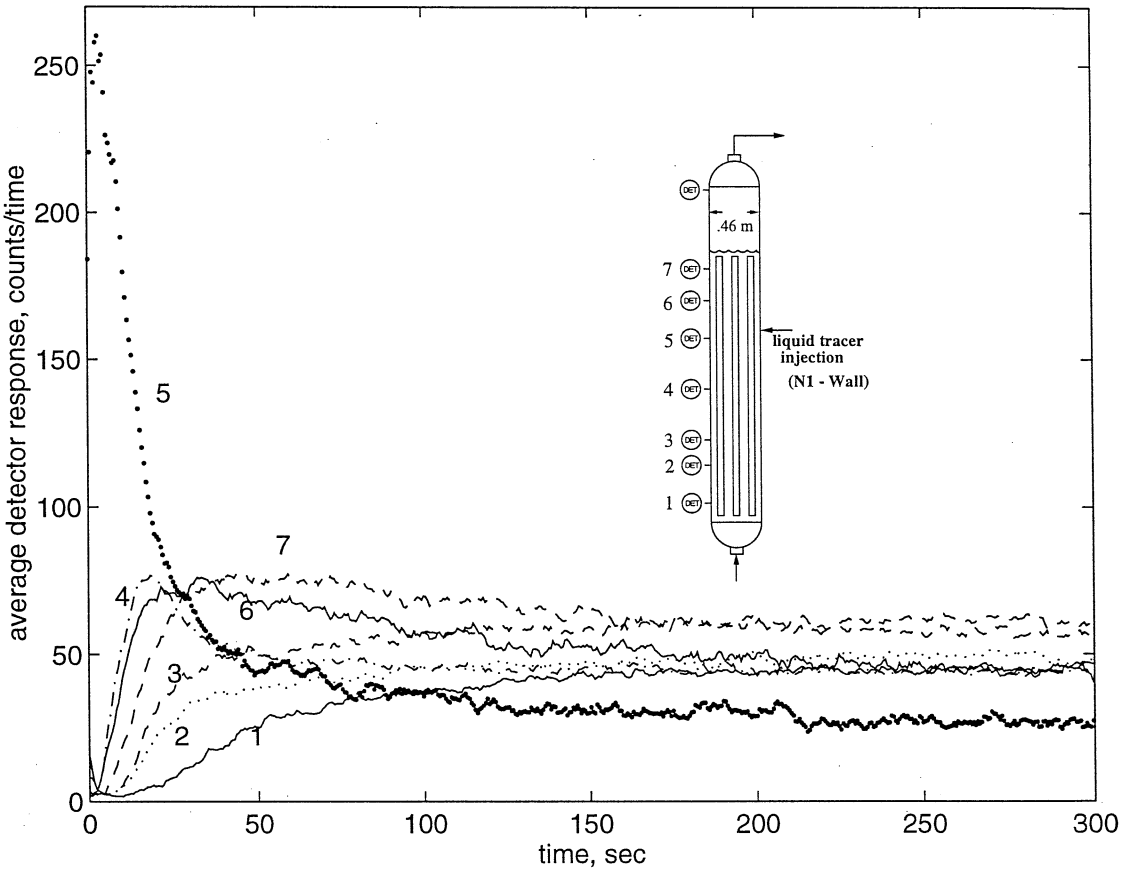

Figure 6.15: Experimental Detector Responses for Wall Injection at Level N1 for Run 14.6

experimental detector response, the local tracer concentration, in a two dimensional axisymmetric domain, $C(r, z, t)$, is first integrated along the radial path r through the column center, using the Beer-Lambert law, to yield a representative radioactive tracer response at a given axial location, $\check{C}(z, t)$. Therefore,

$$\check{C}(z,t) = \int_{r'=0}^{r'=R} C(r', z, t) \exp(-\int_{r'}^{R} \mu_{eff}(r'')dr'')dr' \tag{6.24}$$

where

$$\mu_{eff}(r) = \mu_g \epsilon_g(r) + \mu_{sl}\epsilon_{sl}(r) \tag{6.25}$$

$\check{C}(z, t)$ represents the response measured by the shielded and collimated detectors, which have been used for the present experiments. Since the detectors are collimated,

the only significant contribution of the radiation that is measured comes from the tracer along the radial path r through the column center. Hence, the contribution from the angular and axial direction is neglected in the calculations. The Mn^{56} particles emit γ radiation at 0.85 MeV. The catalyst loading in the reactor for all the three runs was kept at a constant of 40 % by weight. For a given composition of the catalyst particles resulting in a bulk density $\rho_s = 2.02$ gm/cm^3, and liquid (hydrocarbon oil) density of $\rho_l = 0.667$ gm/cm^3, the linear attenuation coefficient of the slurry at 0.85 MeV is $\mu_{sl} = 0.06728$ cm^{-1}, and $\mu_g = 1.0\text{e-}5$ cm^{-1}.

Figures 6.16 and 6.17 show the comparison of model predictions with the experimental tracer responses for the wall injection at level N1 for Run 14.6. The responses have been normalized with respect to their maximum for the sake of comparison. The results show that the model is able to capture the characteristic overshoots as seen by the detector responses at all the measurement levels. A quantitative comparison of the tracer responses is unfortunately not possible due to the fact that the experimental data do not level off at large times at the same height for all the detectors.

Figures 6.18 and 6.19 show the comparison between model predictions and experimental detector responses for the center injection at level N2, and Figure 6.20 for the center injection at level N1. Experimental data at Levels 5,6 and 7 for center injection at N1 and all levels for the wall injection at N2, in Run 14.6 were not available for comparison. For all the different locations of injection, since the operating process conditions are the same, the input model parameters are fixed. Therefore with a consistent set of model parameters the model is able to capture the internal liquid (slurry) and overall mixing in the AFDU reactor, as measured by the detector responses at all the seven locations. Table 6.3 shows the list of the average input parameters calculated for all the three experimental conditions considered. The radial profiles for liquid velocity and turbulent diffusivities are obtained using the procedure described above.

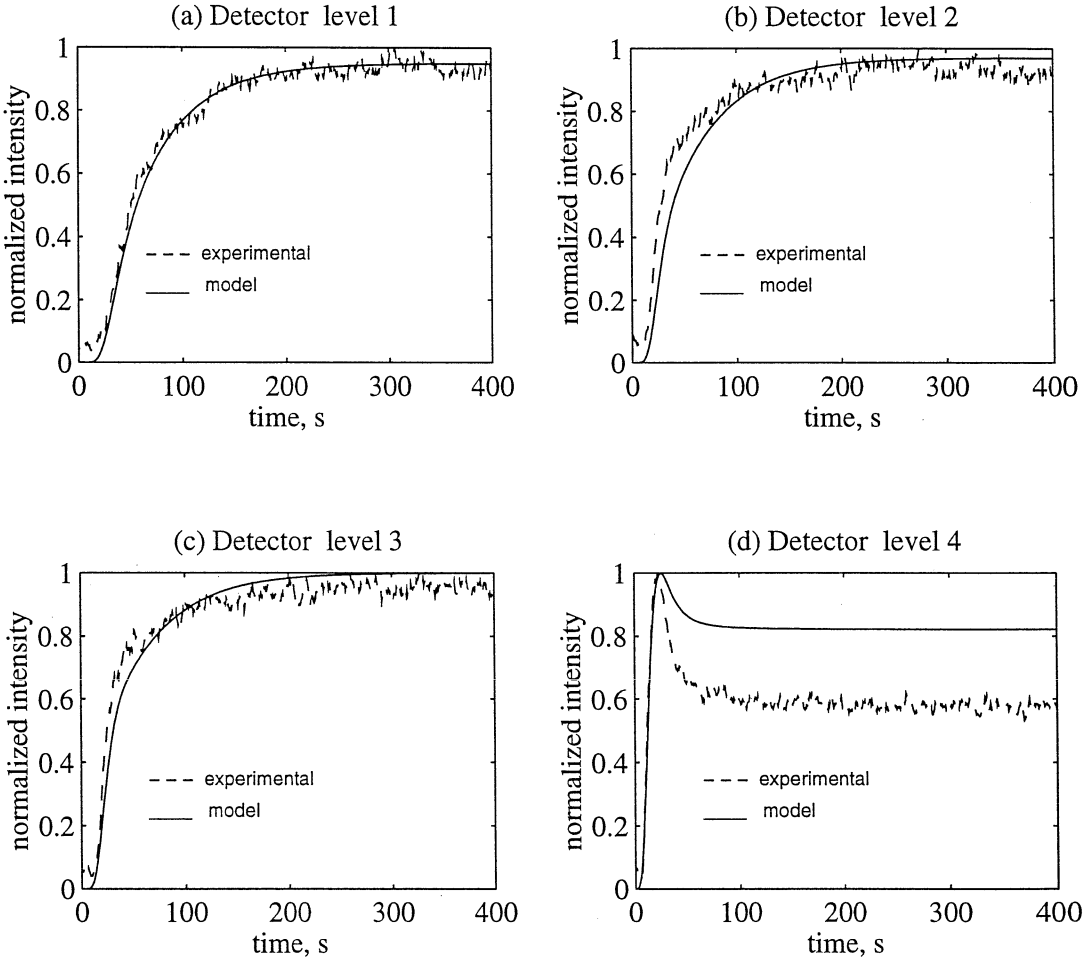

Figure 6.16: Comparison of Model Prediction with Experimental Detector Responses for Wall Injection at Level N1, Run 14.6

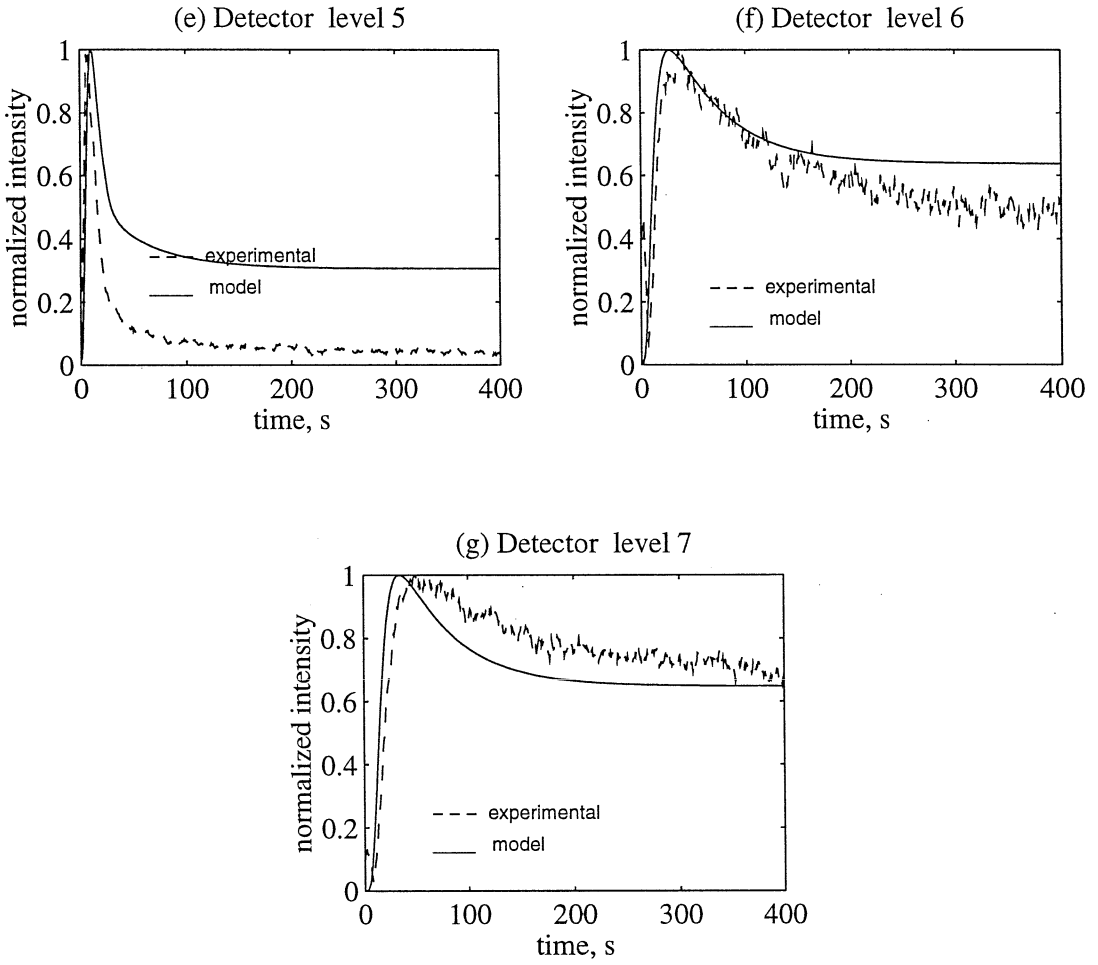

Figure 6.17: Comparison of Model Prediction with Experimental Detector Responses for Wall Injection at Level N1, Run 14.6

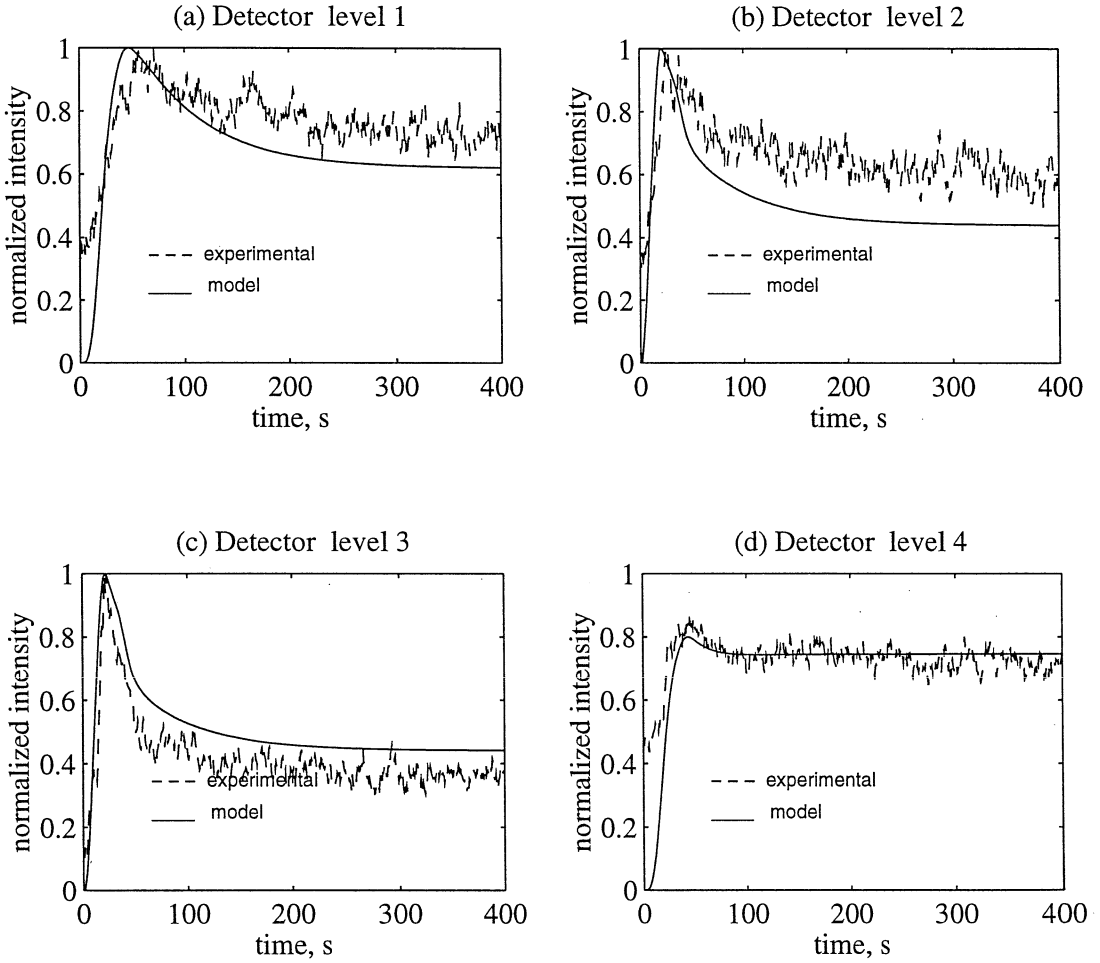

Figure 6.18: Comparison of Model Prediction with Experimental Detector Responses for Center Injection at Level N2, Run 14.6

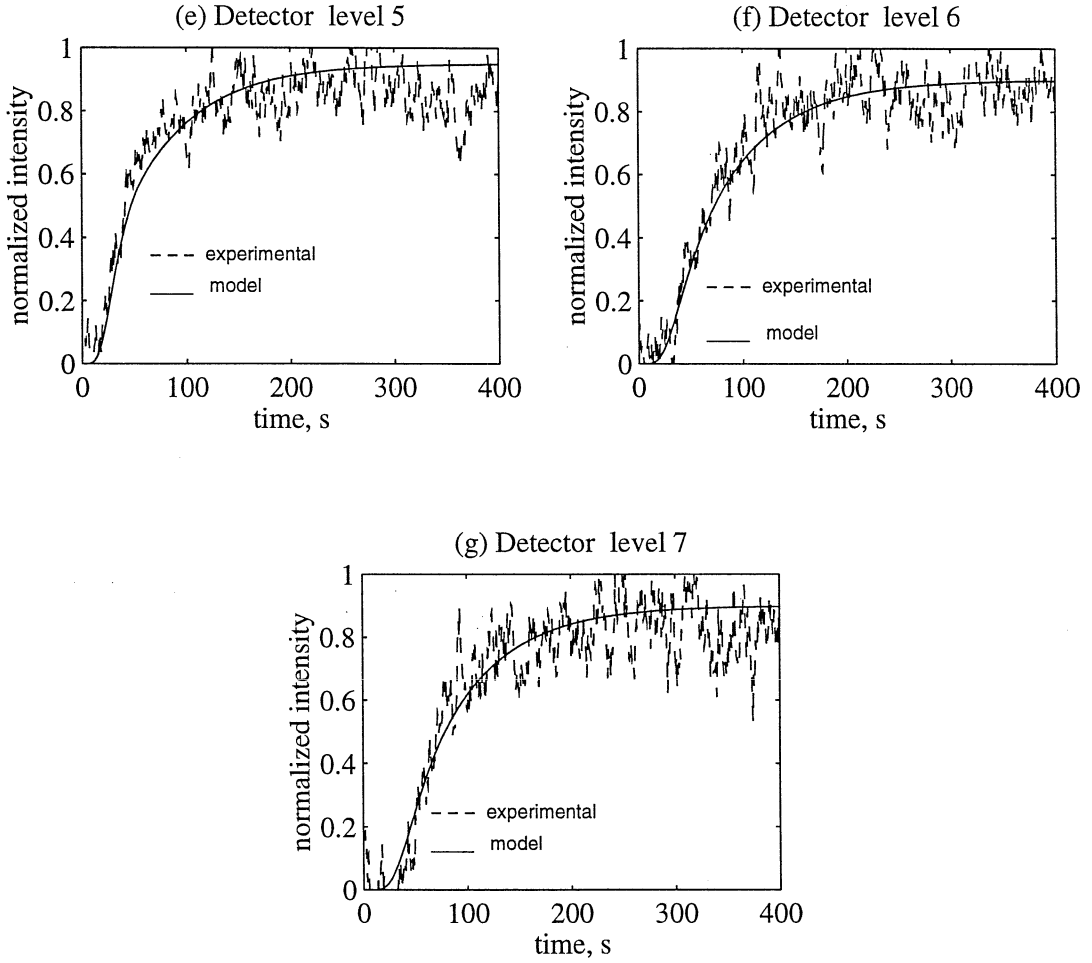

Figure 6.19: Comparison of Model Prediction with Experimental Detector Responses for Center Injection at Level N2, Run 14.6

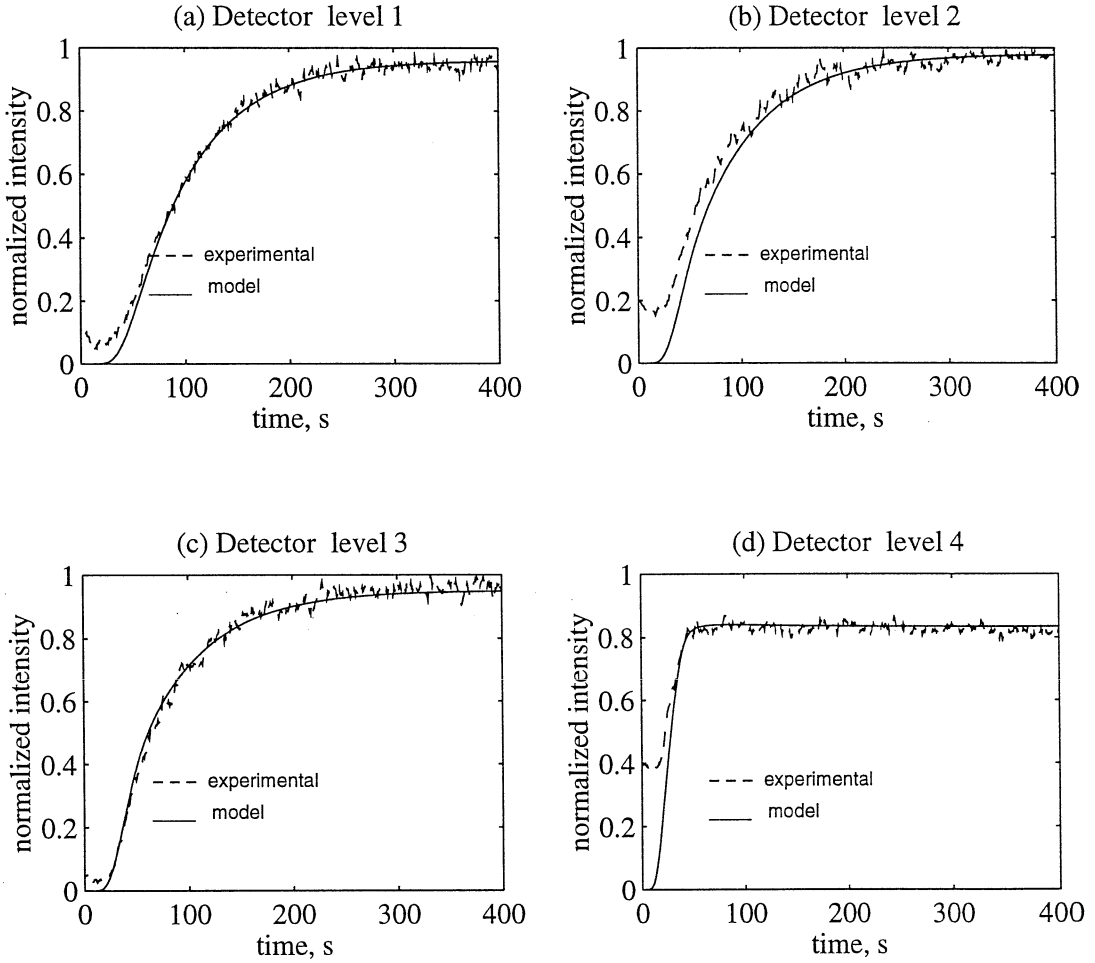

Figure 6.20: Comparison of Model Prediction with Experimental Detector Responses for Center Injection at Level N1, Run 14.6

Table 6.3: List of Estimated Average Fluid Dynamic Parameters for LaPorte AFDU during Methanol Synthesis

Run No.	U_{g0} cm/s	$\bar{\epsilon}_g$	U_{ge} cm/s	$\bar{u}_{rec}$ cm/s	$\overline{D}_{zz}$ cm^2/s	$\overline{D}_{rr}$ cm^2/s
14.6	25.0	0.39	47.4	47.6	965.2	114.1
14.7	14.0	0.33	33.1	41.2	854.0	100.7
14.8	36.0	0.38	44.7	46.5	946.0	111.3

It is to be noted that while Runs 14.6 and 14.7 are at a higher pressure of 52 atm, Run 14.8, which is carried out at a higher superficial gas velocity of 36 cm/s, is at a lower pressure of 36 atm. The effect of pressure is evident in the gas holdup measurements, which indicate a lower holdup for Run 14.8 in comparison with Run 14.6, although it is operated at a higher superficial gas velocity.

The results of the model predictions for the various injections of Runs 14.7 and 14.8 are shown in Appendix F. It is clear from these figures that the model is, in general, able to correctly predict the mixing patterns within the reactor shown by the detector responses. By using a single set of input parameters (Table 6.3) for a given experimental condition, the model is able to capture the mixing patterns for the various injection locations, as measured by detectors at all levels. This substantiates using the proposed convective-diffusion model to describe liquid mixing based on liquid recirculation and turbulence, and suggests that the preliminary scale-up rules developed result in a good estimate of the input fluid dynamic model parameters. Such comparisons indirectly justify the proposed methodology of characterization of churn-turbulent bubble columns, by using the gas holdup in the reactor as a means of accounting for the effects of pressure, solids and other system parameters.

The approach used for evaluation of the model parameters stresses the importance of measurement and prediction of the gas holdup and its radial distribution in the column. Several correlations exist in the literature that account for the effect of pressure and liquid properties on overall gas holdup. However, there is no good agreement between the correlations, even at atmospheric pressure, as discussed

in Chapter 2. A combination of the correlations of Wilkinson et al. (1992) for the transition holdup and velocity (1T. in Table 2.1), along with that of Krishna and Ellenberger (1996) for the dilute phase holdup (2L. in Table 2.2), seems to yield the best estimates for the global gas holdup in comparison to experimental data in the AFDU during methanol synthesis (Table 6.1). The slurry phase properties existing under experimental conditions in the AFDU are considered, instead of the liquid (except for the surface tension, σ, since no data was available for the slurry), resulting in gas holdups reported in in Table 6.4. The estimated values of the overall gas holdups show reasonable agreement with the measured average holdups, especially at the two higher gas velocities. The estimated transition gas velocity from bubbly flow to churn-turbulent flow, however, seems rather low when compared with experimental results for atmospheric air-water systems. This is partly due to the high values of the holdup of the small bubbles. The high holdup of small bubbles (transition holdup), which is the same for Runs 14.6 and 14.7, results in a higher value of the gas holdup for Run 14.7 ($U_g = 14.0$ cm/s), when compared with experimental measurements.

The correlations of Wilkinson et al. (1992) yield much higher values for the large bubble holdup (1L. in Table 2.2). This is probably since the correlation does not take into consideration the effect of column diameter on the large bubble holdup (which is supposed to decrease with increase in column diameter). Reilly's correlation (2T. in Table 2.1), which resulted in moderate estimates of the transition gas velocity and holdup under atmospheric conditions (Chapter 2), greatly overpredicts the transition holdup for the present high pressure data. For example, for Run 14.6, the transition holdup calculated from Reilly's correlation gives $\epsilon_{trans} = 0.58$, which is much higher than the overall gas holdup measured in the reactor, ~ 0.4. This points to the disparity in the available correlations, which perform well only under a certain range of operating and process conditions.

Correlations such as those presented above are useful in estimating the global gas holdup. There is still no way (empirical or theoretical) of predicting the holdup

Table 6.4: Estimation of Global Gas Holdup in the Reactor Using Correlations from the Literature

Run No.	U_{g_0} cm/s	Press. MPa	Wilkinson (1992) ϵ_{trans}	Wilkinson (1992) U_{trans} (m/s)	Krishna et al. 1996 ϵ_{lb}	Krishna et al. 1996 $\bar{\epsilon}_g$	Measured $\bar{\epsilon}_g$
14.6	25.0	5.2	0.279	0.056	0.120	0.399	0.39
14.7	14.0	5.2	0.279	0.056	0.073	0.353	0.33
14.8	36.0	3.6	0.241	0.049	0.158	0.398	0.38

profiles in the reactor. For such situations, global holdup measurements from DP and NDG prove to be helpful in calculating a holdup profile, as discussed earlier.

6.1.4 Summary

The two dimensional axisymmetric convection-diffusion model provides a good representation of internal liquid mixing in bubble columns. Although the instantaneous flow in bubble columns is highly turbulent and transient in nature, and the time-averaged velocity profile does not exist in the column at any instant in time, by properly accounting for the churn-turbulent flow via the turbulent eddy diffusivities, the model is able to capture, in a statistical sense, the large scale transient flow patterns in the column, thereby yielding the characteristic overshoots seen by the detectors at various axial locations. This represents the meso-scale and macro-scale mixing in the column, which is of importance for modeling bubble column reactors. Results also imply that CARPT measurements for the turbulent eddy diffusivities can provide suitable closure for the $\langle \vec{u}'C' \rangle^x$ terms appearing in the original balance equations. Such model predictions for liquid mixing in bubble columns are the first of their kind, and are truly 'predictions', involving no fitting parameters. The developed model, along with experimental input for the model parameters, therefore allows us to study the influence of fluid dynamics on liquid mixing in bubble columns.

The scale-up strategy proposed in Chapter 5 for evaluating the model parameters in the AFDU slurry bubble column reactor during methanol synthesis, results

in fairly good predictions of the characteristic mixing times within the column as measured by the radiation detectors at various axial locations. This indirectly substantiates the proposed methodology of using the gas holdup in churn-turbulent flows, at sufficiently high gas velocities, for characterizing the systems of interest.

6.2 One Dimensional Recirculation with Cross Flow and Dispersion Model

In the previous section it was shown that the two dimensional axisymmetric convection-diffusion model derived from the fundamental species balance equation, and utilizing experimental data from CARPT and CT for the fluid dynamic model parameters, is able to characterize liquid mixing in bubble columns. This establishes the validity of using long time averaging for the fluid dynamic parameters, in order to describe the macro-scale transient tracer distribution characteristics in the column. The objective of this section is to study if a simplified one dimensional version of the original two dimensional model, with appropriate fluid dynamic parameters, can be successfully used to describe liquid mixing in bubble columns. For this purpose a one dimensional recirculation with cross flow and turbulent dispersion model (RCFDM) (also referred to as the two compartment convective-diffusion model) is developed and solved.

6.2.1 Development of Model Equations for RCFDM

The original two dimensional model given by Equation 6.9, when rewritten for the middle region of the flow domain becomes

$$\frac{\partial(\epsilon C)}{\partial t} + \frac{\partial}{\partial z}(\epsilon u_z C) = \frac{1}{r}\frac{\partial}{\partial r}[r\epsilon D_{rr}\frac{\partial C}{\partial r}] + \frac{\partial}{\partial z}[\epsilon D_{zz}\frac{\partial C}{\partial z}] \tag{6.26}$$

In the above equation, the radial convection term on the left hand side of Equation 6.9 has been dropped, since the radial velocities in the middle section of the column are negligible and the flow is one dimensional. In order to reduce the two dimensional

model to one dimension, the above equation is discretized in the radial direction only, by dividing the domain into two finite volume cells (finite volume representation), as shown in Figure 6.21. This results in two equations.

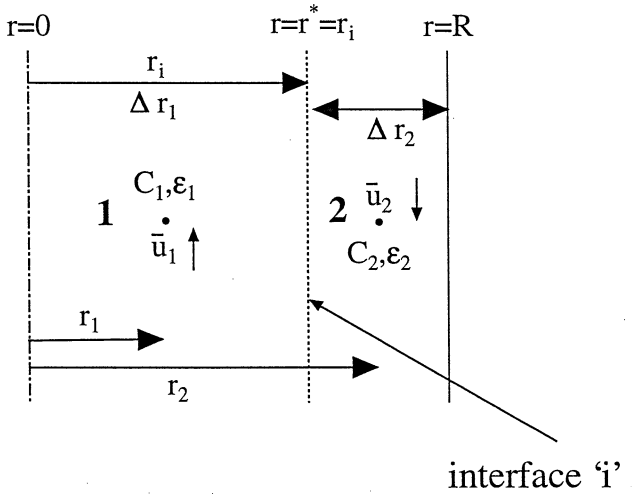

Figure 6.21: Finite Volume Discretization of the Flow Domain in the Radial Direction

For cell 1:

$$r_1\Delta r_1[\frac{\partial}{\partial t}\epsilon_1 C_1 + \frac{\partial}{\partial z}\epsilon_1\overline{u}_1 C_1] = r_1\Delta r_1[\epsilon_1\overline{D}_{zz1}\frac{\partial^2}{\partial z^2}C_1] + (r_i\epsilon_i\overline{D}_{rri})\frac{(C_2 - C_1)}{\Delta r_{12}} \qquad (6.27)$$

where Δr_{12} is the distance between the two nodes 1 and 2. Since for the present case the nodes are placed in the center of each control volume,

$$\Delta r_{12} = (\frac{\Delta r_1 + \Delta r_2}{2}) \qquad (6.28)$$

Hence, Equation 6.27 simplifies to

$$r_1\Delta r_1[\frac{\partial}{\partial t}\epsilon_1 C_1 + \frac{\partial}{\partial z}\epsilon_1\overline{u}_1 C_1] = r_1\Delta r_1[\epsilon_1\overline{D}_{zz1}\frac{\partial^2}{\partial z^2}C_1] + (r_i\epsilon_i\overline{D}_{rri})\frac{(C_2 - C_1)}{(\frac{\Delta r_1+\Delta r_2}{2})} \quad (6.29)$$

Similarly for cell 2:

$$r_2\Delta r_2[\frac{\partial}{\partial t}\epsilon_2 C_2 - \frac{\partial}{\partial z}\epsilon_2\overline{u}_2 C_2] = r_2\Delta r_2[\epsilon_2\overline{D}_{zz2}\frac{\partial^2}{\partial z^2}C_2] - (r_i\epsilon_i\overline{D}_{rri})\frac{(C_2 - C_1)}{(\frac{\Delta r_1+\Delta r_2}{2})} \quad (6.30)$$

In the above two equations the interface i between cell 1 and 2, is chosen to lie at the point of flow inversion in the column. Cell 1 represents the upflow region and cell 2, the downflow region. The liquid velocities, $\overline{u}_1$ and $\overline{u}_2$ represent the cross-sectional averages of the axial liquid velocity profile, $u_z(r)$, in cell 1 and cell 2, respectively. $\overline{D}_{zz1}$ and $\overline{D}_{zz2}$ denote the cross-sectional averages of the axial eddy diffusivity, D_{zz}, in cells 1 and 2, respectively. $\overline{D}_{rri}$ is the radial diffusivity at the inversion point, obtained by averaging D_{rr} in the region of the inversion point (few experimental data points closest to the inversion point). Simplifying Equations 6.29 and 6.30, we arrive at the following equations for the upflow and downflow region:

$$\frac{\partial}{\partial t}C_1 + \frac{\partial}{\partial z}\overline{u}_1 C_1 = D_1\frac{\partial^2}{\partial z^2}C_1 - \frac{D_{ri}}{a_1}(C_1 - C_2) \quad (6.31)$$

$$\frac{\partial}{\partial t}C_2 - \frac{\partial}{\partial z}\overline{u}_2 C_2 = D_2\frac{\partial^2}{\partial z^2}C_2 + \frac{D_{ri}}{a_2}(C_1 - C_2) \quad (6.32)$$

where

$$a_1 = (\frac{\epsilon_1}{\epsilon_i})\frac{r^*}{4}R \quad (6.33)$$

$$a_2 = (\frac{\epsilon_2}{\epsilon_i})\frac{(R^2 - r^{*2})}{4r^*}R \quad (6.34)$$

$$D_1 = \overline{D}_{zz1} \quad (6.35)$$

$$D_2 = \overline{D}_{zz2} \quad (6.36)$$

$$D_{ri} = \overline{D}_{rr} \quad (6.37)$$

r^* is the radial position of flow inversion (Figure 6.21), ϵ_1 and ϵ_2 are the average liquid holdups in cells 1 and 2, and ϵ_i is the liquid holdup at the inversion point.

The RCFDM thus phenomenologically accounts for the contributions of liquid recirculation and turbulent interaction in describing liquid mixing in bubble columns. The above model equations represent the middle fully developed region, with liquid flowing upward in the core section 1 and flowing downward in annular section 2, between the core and the walls. Superimposed on this convective recirculation is the mixing caused by the random turbulent fluctuating motion of the fluid elements, caused by the passage of the rising bubbles, which gives rise to axial dispersion in each leg and radial exchange between the upflow and downflow sections. This turbulent axial mixing is accounted for by D_1 and D_2, and the radial mixing is incorporated in terms of the radial eddy diffusivity D_{ri}, at the interface between cell 1 and cell 2. Since the magnitude of the axial eddy diffusivities $D_{zz}(r)$ is, in general, relatively high, it is assumed that the contribution of the velocity profile to axial dispersion in each leg is negligible. Therefore, D_1 and D_2 are considered to truly represent axial eddy diffusion (Equations 6.35 and 6.36), which contribute to turbulent axial mixing in cells 1 and 2. The validity of this assumption is checked later on when comparing the model predictions with experimental data. Equations 6.31 and 6.32 are similar to the model equations which were originally developed (Degaleesan et al. 1996), based on heuristic arguments and utilized a cross flow coefficient, K, as a fitting parameter instead of D_{ri}. This model is a variation of the recycle and cross flow model of Hochman and McCord (1970) and can be considered also as an extended version of the model of Wilkinson et al. (1993).

The end zones of the middle region, where the liquid turns around, are connected to perfectly mixed tanks. The equations for these well mixed regions, A and B (Figure 6.22), are, respectively:

$$V_a \bar{\epsilon}_a \frac{dC_a}{dt} = F_0 C_0 - F_1 C_a + F_2 C_2|_{z=0} \tag{6.38}$$

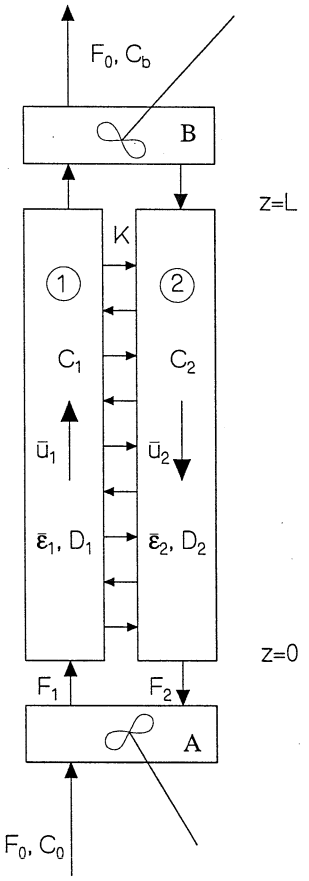

Figure 6.22: Schematic of Recirculation with Cross Flow and Dispersion Model (RCFDM)

$$V_b \bar{\epsilon}_b \frac{dC_b}{dt} = F_1 C_1|_{z=L} - F_2 C_b - F_0 C_b \tag{6.39}$$

where F_0 is the inlet liquid volumetric flow rate to the column, and F_1 and F_2 are the liquid volumetric flow rates in the upflow section 1 and downflow section 2, respectively. Initial conditions for a step input of tracer at the bottom of the column are:

$$C_0 = H(t) \quad \text{and} \quad C_1 = C_2 = C_a = C_b = 0 \quad @t = 0 \tag{6.40}$$

Boundary conditions for the upflow region are given by Equations 6.41 and 6.42 and for the downflow region by Equations 6.43 and 6.44:

For the upflow section:

$$\bar{u}_1 C_a = \bar{u}_1 C_1|_{z=0} - D_1 \frac{\partial C_1}{\partial z}|_{z=0} \tag{6.41}$$

$$\frac{\partial C_1}{\partial z}|_{z=L} = 0 \tag{6.42}$$

For the downflow section:

$$\bar{u}_2 C_b = \bar{u}_2 C_2|_{z=L} + D_2 \frac{\partial C_2}{\partial z}|_{z=L} \tag{6.43}$$

$$\frac{\partial C_2}{\partial z}|_{z=0} = 0 \tag{6.44}$$

The heights of the two well mixed regions A and B are assumed to be equal to the diameter of the column. The basis for this assumption is the experimental observations obtained from CARPT measurements, which suggest that in these regions of the column, radial velocities are quite significant (10 to 15 cm/s in a 19 cm diameter column) and the liquid turbulence is significantly high (turbulent diffusivities are about 1.5 to 2 times the values in the middle section of the column).

The input fluid dynamic parameters to the model, $\overline{u}_1$, $\overline{u}_2$, $\bar{\epsilon}_1$, $\bar{\epsilon}_2$, D_1, D_2 and D_{ri} are obtained from experimental measurements using CARPT and CT. The model equations are solved using implicit finite differences with backward differences in spatial coordinates. Due to the nature of the boundary conditions, an implicit scheme is necessary to solve the system of equations.

The use of the model is illustrated by comparing the model predicted tracer response with the experimental data of Myers et al. (1986), just as was done in the case of the two dimensional model. Using the experimental results form CARPT

and CT, for the one dimensional profiles for axial liquid velocity, liquid holdup and turbulent eddy diffusivities (Figures 6.3, 6.4 and 6.5), the following average values are obtained: $\bar{u}_1 = 12.5$ cm/s, $\bar{u}_2 = 7.7$ cm/s, $\bar{\epsilon}_1 = 0.79$ and $\bar{\epsilon}_2 = 0.88$. These values satisfy continuity within 8%. The cross-sectional averaged axial eddy diffusivities are $D_1 = \overline{D}_{zz1} = 285$ cm^2/s, $D_2 = \overline{D}_{zz2} = 440$ cm^2/s and $D_{ri} = 34$ cm^2/s.

Comparison of RCFDM prediction with experimental tracer response data (Myers et al. 1986), shown in Figure 6.23, is good. Also shown is the two dimensional model prediction, from which it is evident that the two predictions are quite close. The prediction of the RCFDM (based on the variance of the RTD) indicates a slightly lower degree of axial mixing in the column when compared with the two

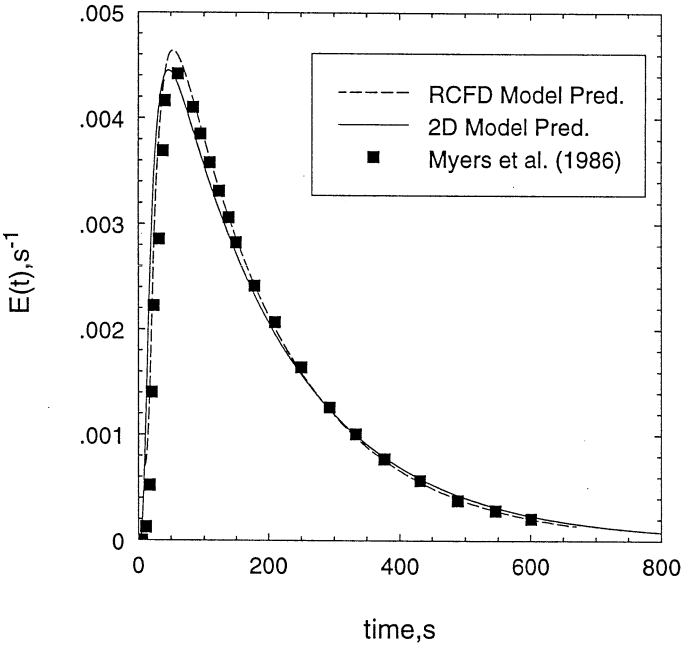

Figure 6.23: Comparison of Experimental Tracer Response with RCFDM Prediction

dimensional convection-diffusion model (slightly higher variance). It is possible that this minor discrepancy is due to the averaging of the axial velocity profile in the upleg and downleg ($\overline{u}_1$ and $\overline{u}_2$) and neglecting the contribution of the radial profile of the axial liquid velocity to axial dispersion in these sections (D_1 and D_2 are considered

to represent axial turbulent diffusion alone). This would imply a lower level of liquid backmixing. However, as is obvious from Figure 6.23, the resulting difference is quite small and may be ignored. The radial exchange between the upflow and downflow sections, which is known to determine the Taylor-type axial diffusivity is still being captured by the RCFDM.

The model is also tested against the radioactive tracer data from the AFDU reactor during methanol synthesis (details of experiments provided in Chapter 6.1.3). The specific condition considered here is Run 14.6 (Table 6.1), for wall injection at level N1 (Figure 6.15). With the present model, the injection at the wall is represented as an injection in the downflow section 2. The model parameters are calculated from the fluid dynamic parameters estimated using the scale-up equations and characterization methodology developed in Chapter 5, discussed in Chapter 6.1.3. and listed in Table 6.5. The comparisons shown in Figures 6.24 and 6.25 indicate that a simplified one dimensional two-compartment convection-diffusion model is also able to capture the characteristic trends in the radioactive tracer data as measured at all the seven detector locations. Although the model is one dimensional, due to the phenomenological representation of the flow it essentially captures the two dimensional effects, and is therefore able to correctly predict liquid mixing within the column.

Table 6.5: Estimated RCFD Model Parameters for the Methanol Synthesis AFDU Reactor Operating at U_g = 25 cm/s, P = 52 atm, T = 250 C (Run 14.6)

$\bar{u}_1$ (cm/s)	47.7	D_1 (cm^2/s)	868.6
$\bar{u}_2$ (cm/s)	37.8	D_2 (cm^2/s)	1042.4
$\bar{\epsilon}_1$	0.464	D_{ri} (cm^2/s)	46.3
$\bar{\epsilon}_2$	0.752		

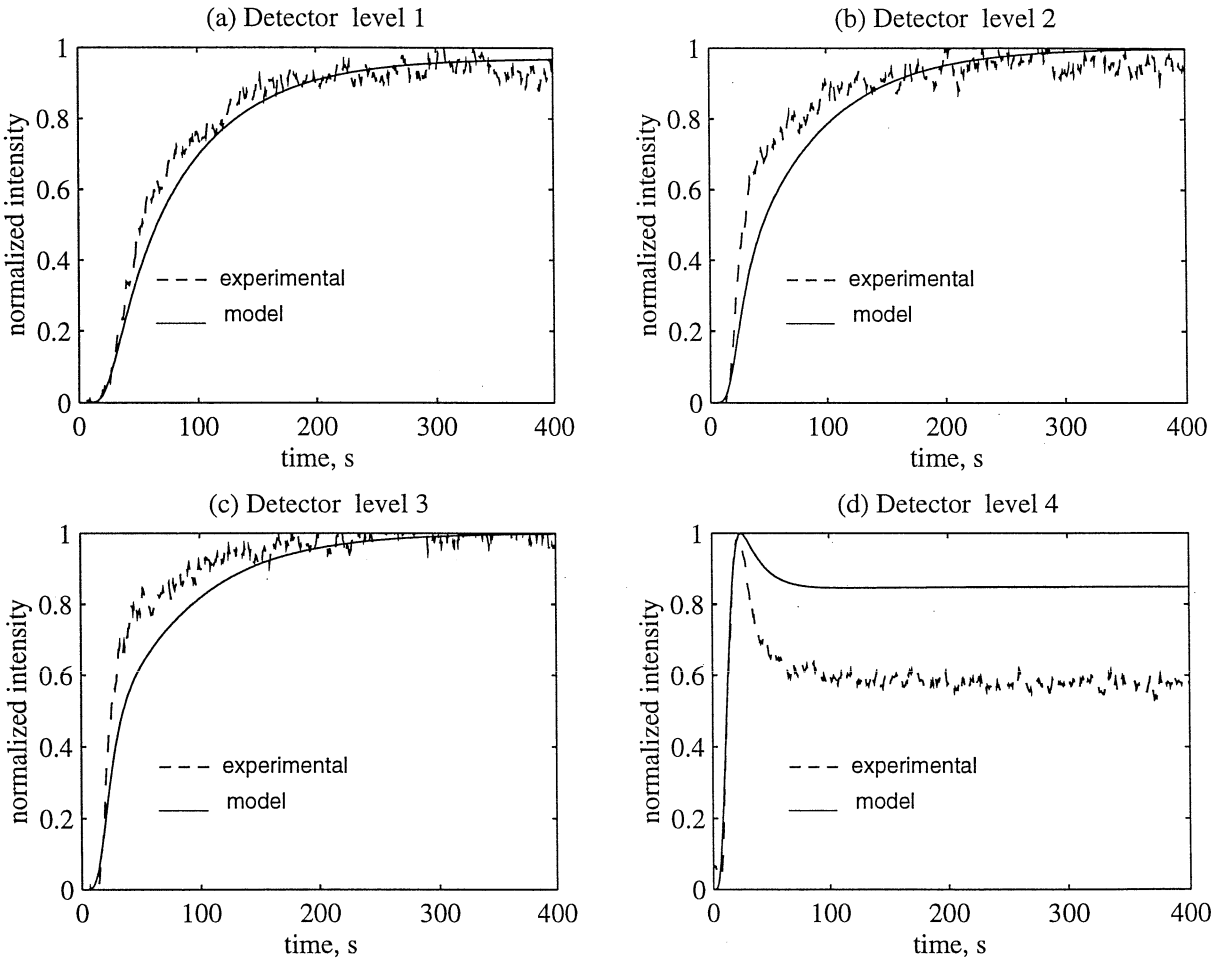

Figure 6.24: Comparison of RCFD Model Prediction with Experimental Detector Responses for Wall Injection at Level N1, Run 14.6

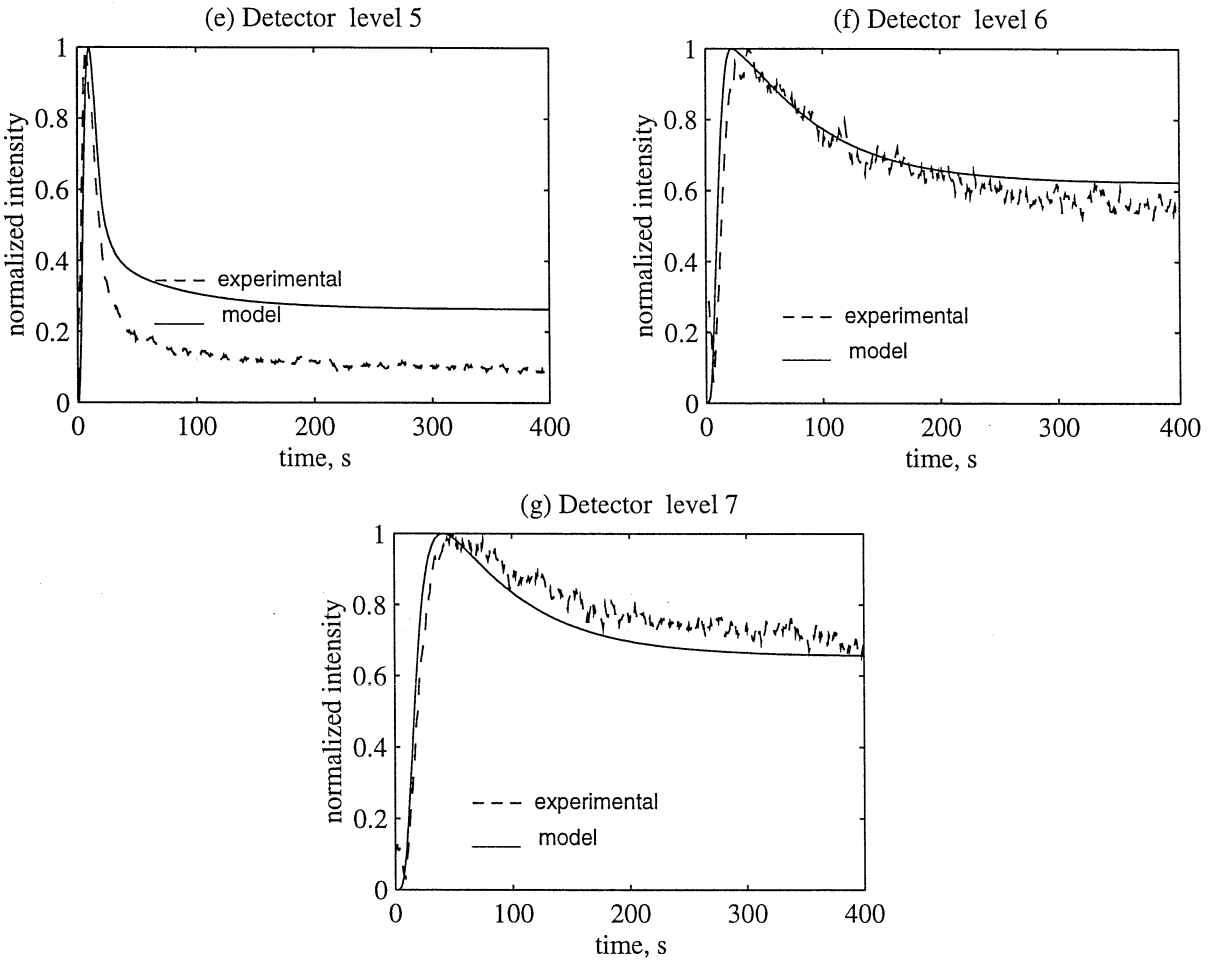

Figure 6.25: Comparison of RCFD Model Prediction with Experimental Detector Responses for Wall Injection at Level N1, Run 14.6

Summary

The simplified one dimensional recirculation with cross flow and dispersion (RCFD) model or the two-compartment convection-diffusion model has been shown to be able to characterize liquid mixing in bubble columns. Having been developed from the original fundamental two dimensional convection-diffusion model, the input fluid dynamic parameters to this model can directly be evaluated from CARPT CT experiments, for laboratory scale bubble columns, and using the scale-up equations (Chapter 5) for industrial scale bubble columns. The advantage of such a model (over the fully two dimensional model) is its computational simplicity. It can be easily extended to examine the behavior of the model in the presence of homogeneous liquid phase reaction. In addition, since liquid recirculation governs the behavior of the gas phase to some extent (small bubbles are considered to be recirculated along with the liquid), it can be applied to study mixing of the gas phase and gas-liquid mass transfer.

An extension of the RCFD model, to include homogeneous liquid phase reaction, is presented in Appendix G for a set of two parallel irreversible reactions. It is shown that there is no significant difference in conversions and selectivities obtained between the RCFDM and the one dimensional Axial Dispersion Model. However, the assumption of complete backmixing of the liquid phase in bubble columns, and using a CSTR model, results in considerable reduction in both conversions and selectivity.

6.3 Contributions of Convection and Turbulence to Liquid Backmixing in Bubble Columns

In this section a Taylor-type analysis of the fundamental two dimensional axisymmetric convection-diffusion equation for liquid mixing in bubble columns is performed, to arrive at an expression for the effective axial dispersion coefficient in terms of the two dominant factors contributing to liquid backmixing, i.e. convective recirculation,

and turbulent eddy diffusion (axial and radial). This will allow us to quantify the contributions of these mechanisms to overall liquid mixing in bubble columns.

This analysis is restricted to systems with low superficial liquid velocities, wherein the cross-sectional average liquid velocity relative to local liquid velocities is negligible. The treatment is based on a steady backmixing experiment in which gas and liquid are introduced at their respective flow rates cocurrently from the bottom of the column and a continuous stream of liquid tracer is introduced uniformly at the top of the column, as illustrated in Figure 6.26. For the purpose of this analysis, the liquid flow rate through the column can be as low as possible, just sufficient enough

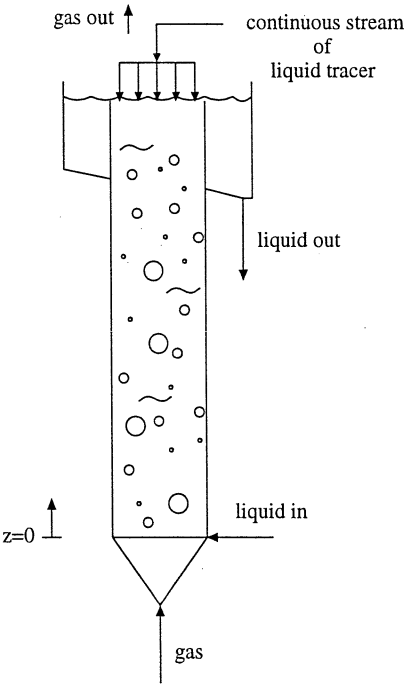

Figure 6.26: Steady Backmixing Experiment

to ensure an outflow of liquid which can carry the tracer. Due to liquid backmixing, a steady axial liquid tracer concentration profile is established in the column. This can be represented by the steady state approximation of the transient two dimensional convection diffusion equation (Equation 6.9), written as:

$$\frac{1}{r}\frac{\partial}{\partial r}\epsilon(r)D_{rr}(r)r\frac{\partial C}{\partial r} = \epsilon(r)u_z(r)\frac{\partial C}{\partial z} - \epsilon(r)D_{zz}(r)\frac{\partial^2 C}{\partial z^2} \tag{6.45}$$

The above equation is written for the well developed region of the flow in bubble columns, where the time averaged axial liquid velocity is a function of radius only and radial velocities are zero. End effects are neglected. This is applicable for bubble columns operating at large length to diameter ratios (≥ 6). Based on the gathered experimental evidence it is also assumed that the turbulent eddy diffusivities in the fully developed region are a function of radial position only.

The liquid tracer concentration $C(r,z)$ is now decomposed into two parts as:

$$C(r,z) \equiv \bar{C}(z) + C'(r) \tag{6.46}$$

where $\bar{C}$ is a function of axial position only and C' is dependent on radial position only. $\bar{C}$ is the cross-sectional average liquid concentration and hence is independent of radial position, r. C' hence represents the concentration variations around the cross-sectional mean, with a cross-sectional average of zero. Simulation results of the steady state two dimensional model (Equation 6.45), shown in Figure 6.27, indicate that C' is only a mild function of z, which is negligible when compared to $\bar{C}$. Hence Equation 6.46 is a good approximation of the actual liquid tracer concentration throughout the column. Equation 6.45 can now be rewritten as

$$\frac{1}{r}\frac{\partial}{\partial r}\epsilon(r)D_{rr}(r)r\frac{\partial C'(r)}{\partial r} = \epsilon(r)u_z(r)\frac{\partial \bar{C}(z)}{\partial z} - \epsilon(r)D_{zz}(r)\frac{\partial^2 \bar{C}(z)}{\partial z^2} \tag{6.47}$$

Experimental evidence from the literature (Ohki and Inoue 1970; Myers 1986) and simulation results (Figure 6.27) show the following dependence of the cross-sectional mean concentration $\bar{C}$ on axial position, z:

$$\bar{C}(z) = C_0 \exp(k_z z) \tag{6.48}$$

where k_z is a constant. Therefore

$$\frac{\partial^2 \bar{C}}{\partial z^2} = k_z \frac{\partial \bar{C}}{\partial z} \tag{6.49}$$

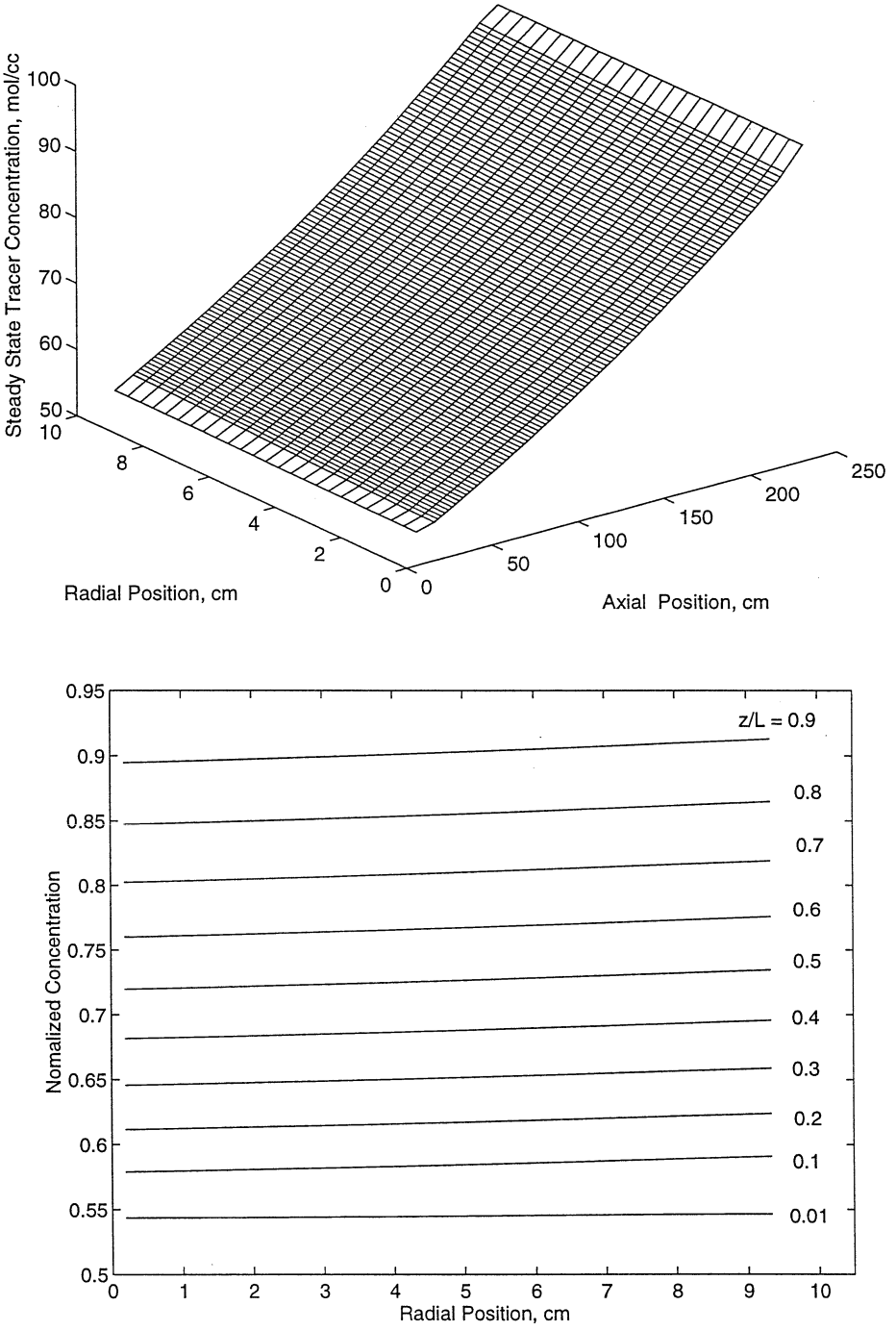

Figure 6.27: Simulation Results of the Steady State Two Dimensional Convection Diffusion Model

By substituting the above result into Equation 6.47 we get:

$$\frac{1}{r}\frac{\partial}{\partial r}\epsilon(r)D_{rr}(r)r\frac{\partial C'(r)}{\partial r} = \frac{\partial \bar{C}(z)}{\partial z}[\epsilon(r)u_z(r) - \epsilon(r)D_{zz}(r)k_z] \tag{6.50}$$

Following a Taylor-type analysis (after double integration over r) with symmetry conditions at the center and zero flux at the wall the following is obtained:

$$C'(r) = \frac{d\bar{C}(z)}{dz}I2(r) \tag{6.51}$$

where

$$I2(r) = \int_0^r \frac{I(r')}{r'\epsilon(r')D_{rr}(r')}dr' \tag{6.52}$$

and

$$I(r) = \int_0^r r\epsilon(r')[u_z(r') - D_{zz}(r')k_z]dr' \tag{6.53}$$

An average flux for a cross-section of the column can now be defined as

$$J = \underbrace{\frac{\int_0^R r\epsilon(r)u_z(r)C(r,z)dr}{\int_0^R r\epsilon(r)dr}}_{T1} - \underbrace{\frac{\int_0^R \epsilon(r)rD_{zz}(r)dr}{\int_0^R r\epsilon(r)dr}\frac{\partial \bar{C}}{\partial z}}_{T2} \tag{6.54}$$

Substituting Equation 6.46 for $C(r,z)$ in the first term of Equation 6.54, the integral involving $\bar{C}$ can be dropped, giving the following expression for $T1$:

$$T1 = \frac{\partial \bar{C}(z)}{\partial z}\frac{\int_0^R r\epsilon(r)u_z(r)I2(r)dr}{\int_0^R r\epsilon(r)dr} = -D_{Taylor}\frac{d\bar{C}_z}{dz} \tag{6.55}$$

The second term in Equation 6.54 can be written as:

$$T2 = \overline{D}_{zz}\frac{d\bar{C}_z}{dz} \tag{6.56}$$

Therefore

$$J = -\frac{\partial \bar{C}(z)}{\partial z}[D_{Taylor} + \overline{D}_{zz}] \tag{6.57}$$

$$D_{eff} = D_{Taylor} + \overline{D}_{zz} \tag{6.58}$$

From the above analysis it is possible to estimate the contributions of convection (Taylor dispersion) and turbulence to the one dimensional axial dispersion coefficient. Since the one dimensional model for liquid recirculation used in this study (Appendix A) does not permit an analytical solution for the liquid velocity profile, the evaluation of the above terms is done by numerically integrating the expressions for the various quantities.

6.3.1 Evaluation of the Effective Axial Dispersion Coefficient, D_{eff}, Using Experimental Results from CARPT and CT

Typical axial liquid velocity profiles and profiles of the radial and axial eddy diffusivities are shown in Chapter 4. Figures 6.28 (a and b) and 6.29 show the effect of operating conditions on $\overline{D}_{zz}$, $\overline{D}_{rr}$ and D_{Taylor}. The data presented in both figures are based on experimental data obtained from CARPT for the turbulent diffusivities and liquid velocities, and from CT for holdup profiles. Based on such experimental data, the following functional form is obtained for D_{Taylor}:

$$D_{Taylor} = \frac{1}{K_T} \frac{\bar{u}_{rec}^2 R^2}{\overline{D}_{rr}} \tag{6.59}$$

where $\bar{u}_{rec}$ is the mean liquid recirculating velocity, defined by Equation 5.3 and K_T is a constant

$$K_T = 14.2 \pm 5.4 \quad (\bar{K_T} \pm 2\sigma_{K_T}) \tag{6.60}$$

The above expression for D_{Taylor} is analogous to the famous Taylor diffusivity (Taylor 1954). Since the magnitude of the radial eddy diffusivity is large, the Taylor

dispersion term in Equation 6.59 contributes only in part to the overall axial dispersion. The axial turbulent diffusivity, as seen in Figure 6.28 (a), also plays a major role in axial liquid mixing, contrary to the assumption of many researchers in their analyses.

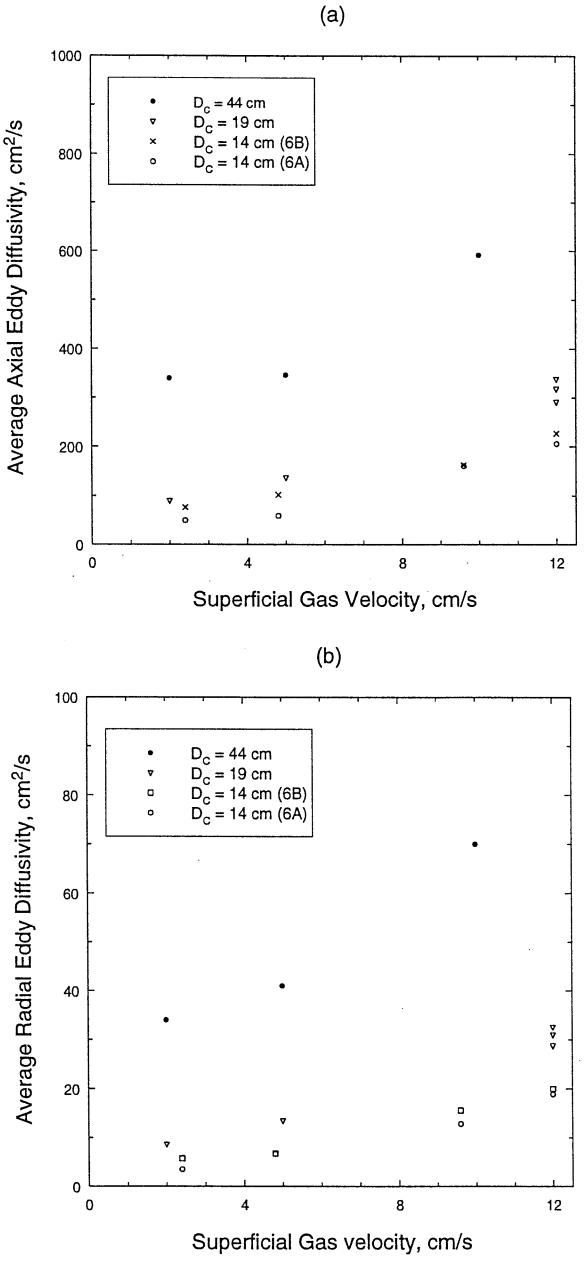

Figure 6.28: Effect of Superficial Gas Velocity on (a) Average Axial Eddy Diffusivity, $\overline{D}_{zz}$, (b) Average Radial Eddy Diffusivity, $\overline{D}_{rr}$

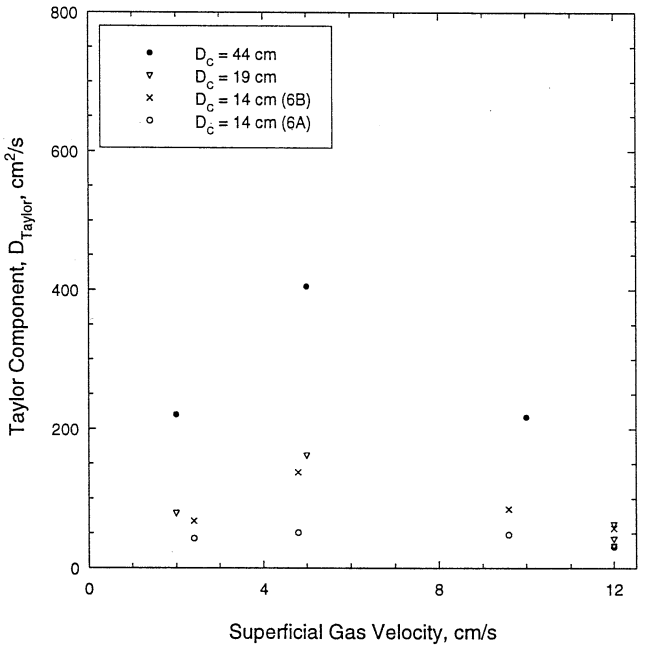

Figure 6.29: Effect of Superficial Gas Velocity on Taylor Component, D_{Taylor}

While there is a monotonic increase of $\overline{D}_{zz}$ (Figure 6.28 (a)) with gas velocity, D_{Taylor} initially increases with gas velocity up to a certain point, beyond which it starts to drop (Figure 6.29). It appears from the data points that this occurs around the transition regime. This trend reflects the behavior of the liquid recirculation ($\overline{u}_{rec}$) and the turbulent eddy diffusivities with gas velocity. At very low gas velocities, convection dominates and the turbulence level is low (as discussed in Chapter 4). Hence, there is initially a strong increase of D_{Taylor} (Equation 6.59) with gas velocity, in the bubbly flow regime. Then, as the gas velocity is increased into the churn-turbulent flow regime, the increase in the turbulent diffusivities starts to become more pronounced (transition from bubbly flow to churn-turbulent flow). This increase in $\overline{D}_{rr}$, relative to $\bar{u}_{rec}$, causes D_{Taylor} to decrease. Figure 6.30 shows the variation of the effective liquid axial dispersion coefficient (obtained from CARPT measurements based on the present analysis) with gas velocity in a 14 cm and 44 cm diameter column. At the lower gas velocities, in the bubbly flow regime, the contribution of

D_{Taylor} to the axial dispersion coefficient is higher than that of $\overline{D}_{zz}$. With further increase in gas velocity the Taylor component decreases. Figure 6.30 shows the trends up to gas velocities of 12 cm/s, for which CARPT data is currently available.

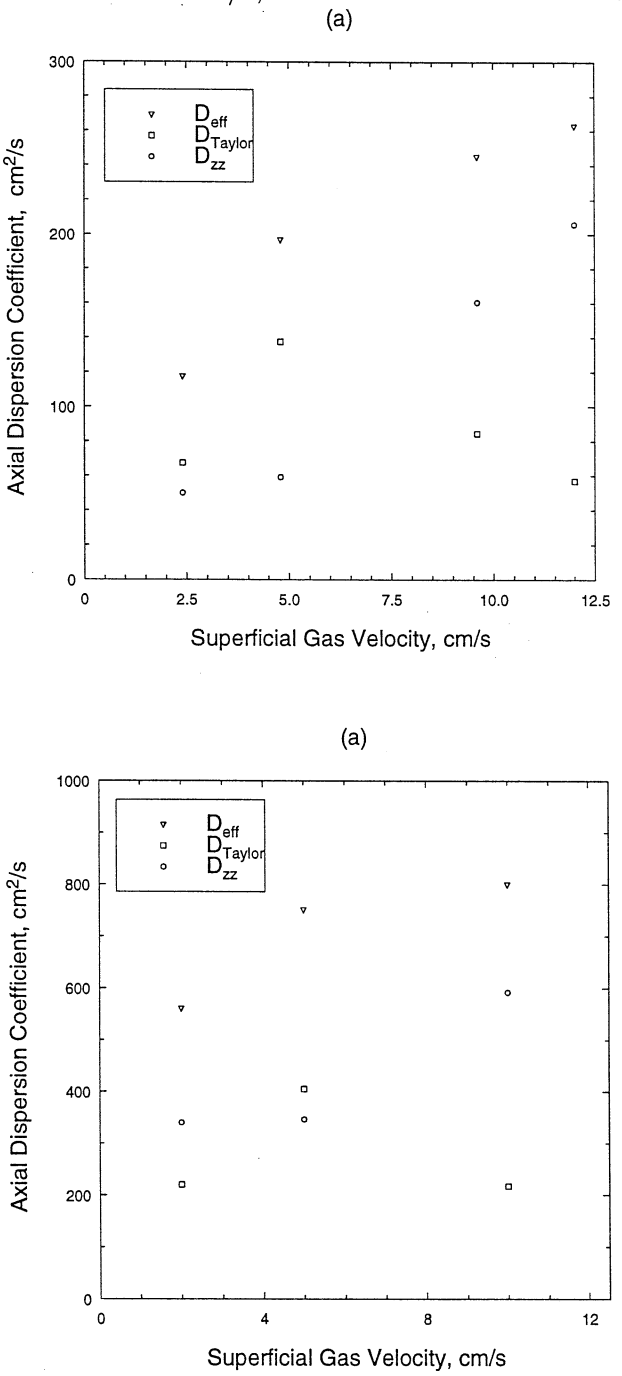

Figure 6.30: Effect of Superficial Gas Velocity on the Axial Dispersion Coefficient and its Contributions, $\overline{D}_{zz}$ and D_{Taylor}, (from CARPT Data) (a) $D_c = 14$ cm (**6A**), (b) $D_c = 44$ cm

The above analysis has therefore resulted in the quantification of the two dominant mechanisms, convective recirculation and turbulence, to liquid backmixing in bubble columns. It is noted that this analysis is only applicable to systems of large L/D aspect ratio, where the flow is fully developed and one dimensional in the middle section of the column, which is in line with the criterion for applicability of the ADM to represent any non-ideal flow pattern. Figure 6.31 shows a good comparison of the effective axial dispersion coefficient, D_{eff}, obtained from CARPT experiments using the present analysis, with the experimentally measured axial dispersion coefficients from the literature, under similar operating conditions.

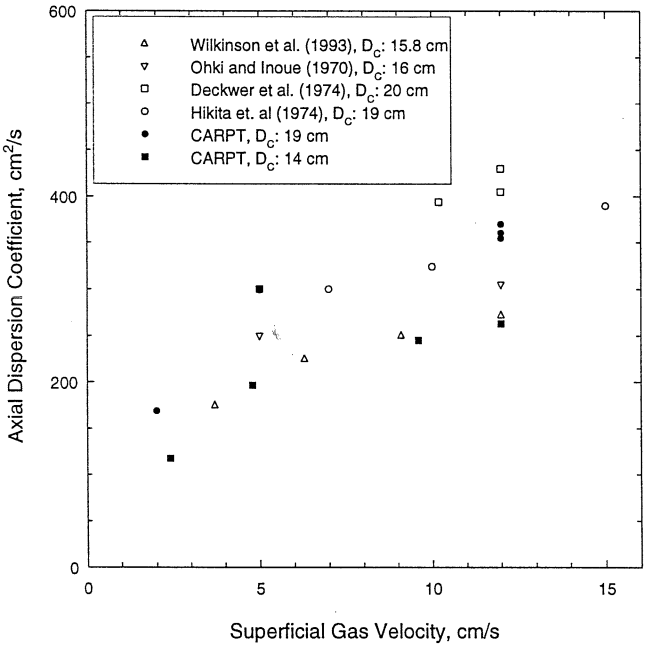

Figure 6.31: Comparison of the Axial Dispersion Coefficients Obtained from CARPT with Experimental Data from the Literature Under Similar Operating Conditions

6.3.2 Prediction of the Liquid Phase Axial Dispersion Coefficient in Large Diameter (> 10 cm) Churn-Turbulent Bubble Columns

Equations 6.58 and 6.59 in conjunction with the scale-up equations (Equations 5.5, 5.8 and 5.9) developed in Chapter 5 for air-water systems at atmospheric conditions, can be directly used to estimate the liquid phase axial dispersion coefficient in churn-turbulent bubble columns beyond the superficial gas velocities for which data is currently available. Such an evaluation for a 19 cm diameter and a 44 cm diameter column results in values of the axial dispersion coefficient as shown in Figures 6.32 and 6.33. It is seen that the axial eddy diffusivity contributes to a larger extent to the overall dispersion coefficient when compared to the Taylor component. This contribution decreases with increase in column diameter. In the churn-turbulent flow regime for which the equations are developed, both the convective and turbulent components to the effective axial dispersion coefficient increase with gas velocity.

For other systems involving different liquid properties (precluding highly viscous liquids), presence of solids, high temperature and pressure, and operating at high superficial gas velocities in the churn-turbulent flow regime, the fluid dynamic parameters ($\bar{u}_{rec}$, $\overline{D}_{zz}$ and $\overline{D}_{rr}$) can be estimated based on an equivalent superficial gas velocity U_{ge}, in air-water atmospheric systems, as described in Chapter 5 (Figure 5.8). The fluid dynamic parameters thus evaluated can be employed along with Equations 6.58 and 6.59 to calculate D_{eff} in systems other than air-water.

The proposed method of estimating the liquid phase axial dispersion coefficient in churn-turbulent bubble columns is tested against experimental data from the literature, under various conditions. The sources of experimental data are listed in Table 6.6) along with the range of operating conditions, of interest here, for which the data are available. Most tracer experiments reported in the literature have been performed in the bubbly flow and transition regime, $U_g \leq 10$ cm/s. Therefore, data in the churn-turbulent flow regime is rather limited.

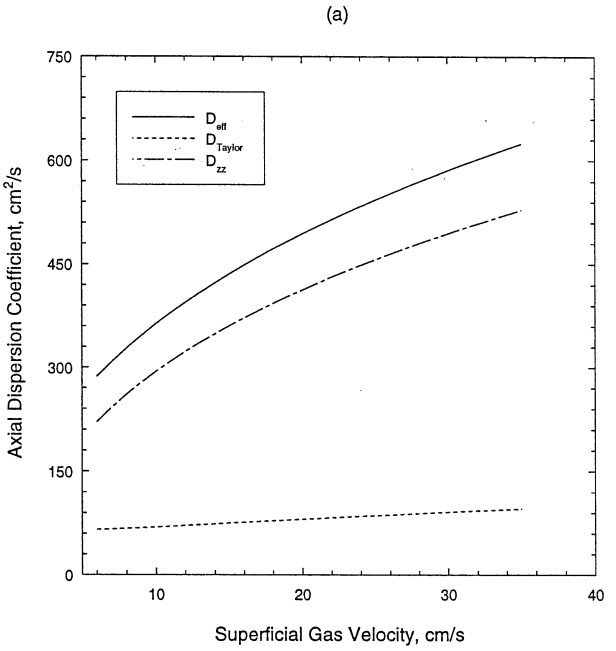

Figure 6.32: Effect of Superficial Gas Velocity on the Axial Dispersion Coefficient and its Contributions in a Column of Diameter 19 cm, Air-Water, Atmospheric System

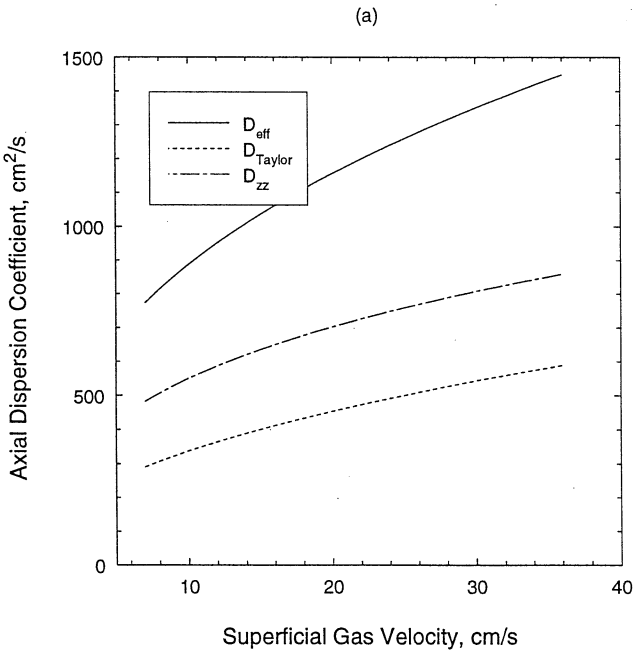

Figure 6.33: Effect of Superficial Gas Velocity on the Axial Dispersion Coefficient and its Contributions in a Column of Diameter 44 cm, Air-Water, Atmospheric System

Table 6.6: Sources of Experimental Data for D_{eff}

Source	D_c cm	U_g cm/s	U_l cm/s	System
Deckwer et al. (1974)	20.0	10.0 - 12.0	0.7	air-water, 1 atm
Goto et al. (1969)	30.0	14.0	"	"
Hikita and Kikukawa (1974)	19.0	20 - 30	0	"
Myers (1986)	19.0	10 - 20	1 - 2	"
Ohki and Inoue (1970)	16.0	15.0 - 25.0	0	"
Reith et al. (1968)	29.0	30.0 - 39.0	1.5	"
Towell and Ackerman (1972)	40.6	8.92	1.2	air-water, 1 atm
Kelkar et al. (1983)	15.4	15.0 - 25.0	0	air-water (electrolyte)
Kara et al. (1982)	15.1	15.0 - 28.0	0	gas-solid-liqd.
Kato et al. (1972)	21.4	15.0 - 20.0	0	"
Kelkar and Shah (1984)	15.4	15.0 - 20.0	0	"
Argo and Cova (1965)	44.8	13 - 20.0	0.72	ammonia synthesis gas -water, high press., hair pin tubes
Degaleesan et al. (1996b)	46.0	15.0 - 36.0	0	gas-solid-liqd., high press., high temp. and internals

The effective liquid axial dispersion coefficient is determined for the various operating conditions listed in Table 6.6. For air-water systems, Equations 6.58 and 6.59 are directly used together with Equations 5.5, 5.8 and 5.9. As an example, consider the experimental conditions of Ohki and Inoue (1970), with $D_c = 16$ cm and for $U_g = 25$ cm/s, for which we find: $\bar{u}_{rec} = 24.2$ cm/s, $\overline{D}_{zz} = 390.2\ cm^2/s$, $\overline{D}_{rr} = 40.3\ cm^2/s$. Substituting the above in Equations 6.59 and 6.58 gives D_{Taylor}= 65.4 cm^2/s and $D_{eff} = 455.6\ cm^2/s$. Figure 6.34 shows a parity plot comparing the effective axial dispersion coefficient predictions based on the present work with experimental data. The circles denote the data for air-water bubble columns under atmospheric conditions.

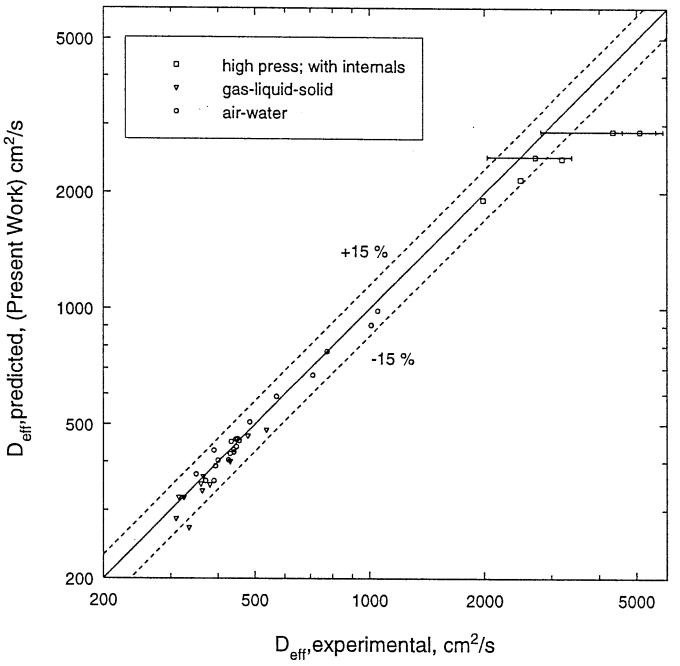

Figure 6.34: Parity Plot Comparing Effective Axial Dispersion Coefficient, D_{eff}, Predicted Using Present Model and Analysis Against Experimental Data From Literature Under Various Conditions

In the presence of solids, that is, for slurry bubble columns, the global gas holdup, reported along with the data for the dispersion coefficients, is used to calculate an equivalent gas velocity, U_{ge}, which is employed to evaluate the axial dispersion coefficient. However, since the gas holdups reported (Kara et al. 1982; Kelkar and Shah. 1984; Kato et al. 1972) are not very different from the gas holdups in air-water systems (Equation 5.2), this does not influence the dispersion coefficient significantly. The solids loading reported in these experiments is less than 20 % by weight. The inverted triangles in Figure 6.34 represent the data for the slurry bubble column experiments. The comparison between experiments and model prediction, in Figure 6.34, is reasonable.

The other set of experimental conditions involves high pressure with internal heat exchanger tubes in the column (Argo and Cova 1965; Degaleesan et al. 1996b). The data of Degaleesan et al. (1996b), for the liquid axial dispersion coefficient, is

for the AFDU slurry bubble column reactor during methanol synthesis, discussed in Chapter 6.1. The high pressure considerably increases the gas holdup in the column and thereby results in a much higher value for U_{ge} when compared with the actual superficial gas velocity (Table 6.3). Due to a corresponding increase in $\bar{u}_{rec}$, $\overline{D}_{zz}$ and $\overline{D}_{rr}$, the overall axial dispersion coefficient, D_{eff}, is higher than its corresponding value at atmospheric pressure. In addition to the effect of pressure, the presence of the internal tubes which span the entire dispersion height also influences liquid (slurry) backmixing, by lowering the extent of radial turbulent mixing, D_{rr}, near the vicinity of the tubes (refer to Equation 6.59). The modified radial profile for the radial eddy diffusivity, such as that shown in Figure 6.13, is cross-sectionally averaged to yield the average radial eddy diffusivity, which is used along with the other estimated fluid dynamic parameters (Table 6.3) to calculate the axial dispersion coefficient. The modified profile for the radial eddy diffusivity reduces the average radial eddy diffusivity to about 40 % of its originally estimated average value. Comparison of the model predicted axial dispersion with experimental data is shown in Figure 6.34. There is a large variation of the experimental dispersion coefficients from their mean values (Degaleesan et al. 1996b), as indicated by the error bars in Figure 6.34. Given the broadness of the error bar in the experimental data, the present method is able to yield a moderate estimate of the liquid axial dispersion coefficient in the AFDU slurry bubble column reactor during methanol synthesis.

The experiments of Argo and Cova (1965) were performed using water and ammonia synthesis gas, in a high pressure column (52 atms) with internals (hairpin tubes). The exact configuration of the heat transfer tubes is not given. However, since the internals are hairpin tubes, same as those in the AFDU reactor (discussed in Chapter 6.1), a similar configuration (Figure 6.14) for 10 hairpin tubes is assumed, to obtain a modified profile for the radial diffusivity, from which the average radial eddy diffusivity is calculated. The presence of the tubes reduces the average radial turbulent diffusivity to about 60 % of its originally estimated value. The axial dispersion coefficients thus estimated are shown in Figure 6.34 to be within about 15

% of the measured values of Argo and Cova (1965). High pressure and the presence of longitudinal internals, therefore increases the axial liquid dispersion coefficient in the column. For example, considering the experimental conditions of Argo and Cova (1965), who used a column of diameter 44.8 cm; at a superficial gas velocity of U_g = 16.2 cm/s, by directly using the scale-up equations (for air-water atmospheric systems) results in D_{eff} = 1091 cm^2/s. By accounting for the effect of high pressure in terms of the global gas holdup, U_{ge} = 49.8 cm/s, which yields a D_{eff} = 1683 cm^2/s. In addition to the high pressure, by taking into consideration the presence of the heat transfer tubes, the axial dispersion coefficient further increases to D_{eff} = 2164.6 cm^2/s, which is the predicted value reported in Figure 6.34. Since most industrial units operate under high pressure and temperature with the presence of internals, it is necessary to account for these effects in estimating the backmixing characteristics in bubble columns and slurry bubble columns.

Most literature correlations for the liquid axial dispersion coefficient in bubble columns (Table 2.4) which were developed for atmospheric systems, tend to severely underpredict the dispersion coefficient for systems operating under high pressure and in the presence of internal tubes. The correlation of Baird and Rice (1975) (Equation 2.46), which is used very frequently in the literature, has been considered as an example here, for evaluation of the dispersion coefficient under the operating conditions given in Table 6.6. A parity plot of the predictions using Equation 2.46 is shown in Figure 6.35. The predictions for the atmospheric systems are good. However, the axial dispersion coefficient for high pressure bubble columns with internals are severely underpredicted by this correlation, and most others reported in Table 2.4. The most probable reason for this is that the data base for the development of the correlations included only atmospheric data.

Recently Berg and Schluter (1995) developed correlations for the axial dispersion coefficient in bubble columns, which accounts for the presence of internals. Their experimental data suggested that longitudinal tubes increase axial phase mixing, based on which they developed the following correlation:

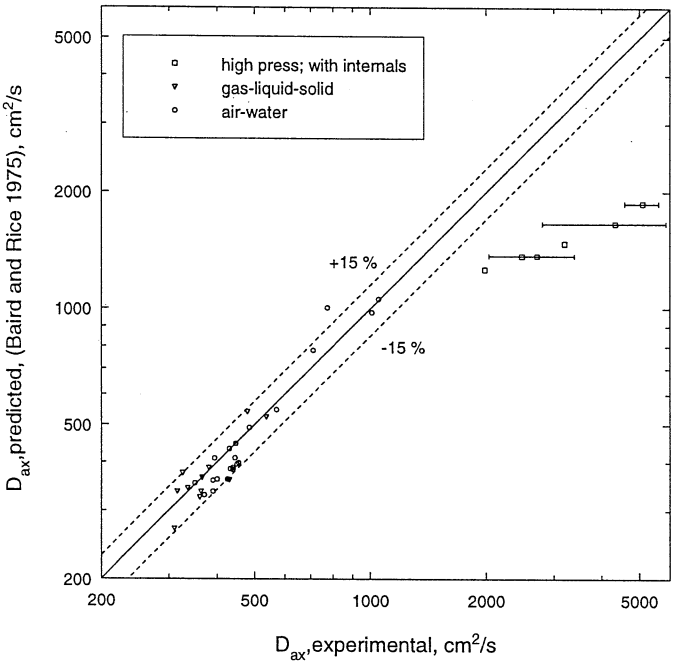

Figure 6.35: Parity Plot Comparing Effective Axial Dispersion Coefficient, D_{eff}, Predicted Using Correlation of Baird and Rice (1975) with Experimental Data From Literature Under Various Conditions

$$D_{ax} = 0.208 U_g^{0.4} (D_c + N_R d_R)^{1.48} \phi_s^{1.8} \nu_l^{-0.12} \qquad \text{SI units} \qquad (6.61)$$

where N_R is the total number of tubes, d_R is the outer diameter of the tubes, ϕ_s is the relative free area and ν_l is the kinematic viscosity of the liquid. In the absence of internals Equation 6.61 is similar to the correlation of Baird and Rice (1975), with a 0.4 power dependence on superficial gas velocity and 1.48 power dependence on column diameter. The parity plot for Berg and Schluter's correlation (Equation 6.61) is shown in Figure 6.36. Figures 6.35 and 6.36 suggest that Equations 2.46 and 6.61 for the atmospheric systems without internals, result in very similar trends for the dispersion coefficient. The only major difference occurs for the high pressure systems with internals. Equation 6.61 of Berg and Schluter (1995), takes into account the presence of internals in the column. However, this equation tends to considerably overpredict the experimentally measured dispersion coefficients. It is possible that

this overprediction arises due to the large power dependence of the axial dispersion coefficient on column diameter. For example, their correlation overpredicts the data of Towell and Ackerman (1972) who used a 40 cm diameter column under atmospheric conditions, by 40 % at $U_g = 8$ cm/s. Unfortunately, there is not sufficient experimental data in large columns, especially in the churn-turbulent flow regime, to verify this conclusively.

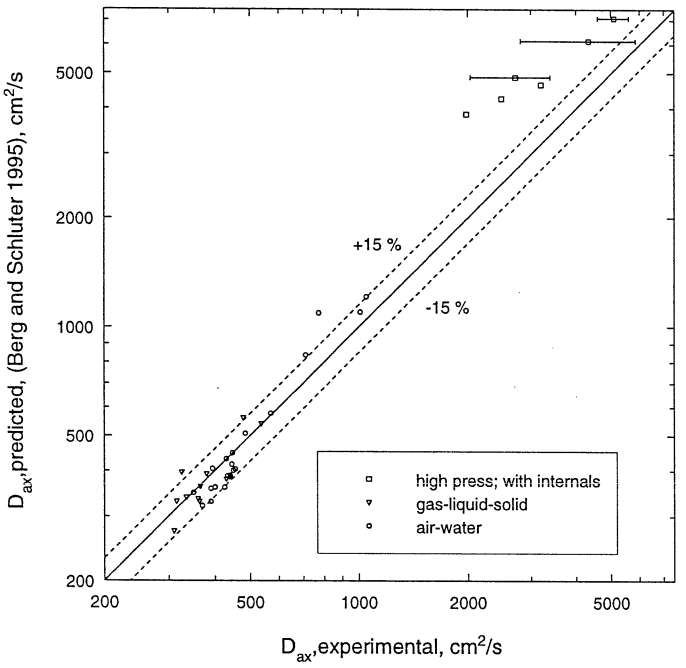

Figure 6.36: Parity Plot Comparing Effective Axial Dispersion Coefficient, D_{eff}, Predicted Using Correlation of Berg and Schluter (1995) with Experimental Data From Literature Under Various Conditions

The present analysis of quantifying the contributions to overall liquid back-mixing in bubble columns, along with the scale-up equations and methodology of characterization of churn-turbulent bubble columns, yields good predictions of the dispersion coefficient in comparison with experimental data, especially under high pressure conditions and with internals. Even though this method also consistently underpredicts the dispersion coefficient under high pressure conditions (Figure 6.34),

the trends in the dispersion coefficient due to the influence of pressure and internals are captured. A quantitatively more accurate prediction may be achieved by experimentally verifying the influence of the internals and high pressure on the fluid dynamic parameters with additional CARPT and CT experiments under various operating conditions at higher gas velocities, and, if necessary, by improving the scale-up equations for these parameters.

Wilkinson et al. (1993) experimentally measured the liquid phase dispersion coefficients in air-water bubble columns at high pressure (5 to 15 atm), and reported an increase in the dispersion coefficients when compared with results obtained under atmospheric conditions. Their experiments were performed at superficial gas velocities less than 15 cm/s. Calculation of swarm velocities (U_g/ϵ_g), for their data (Wilkinson et al. 1993), suggests that for the conditions of their experiments, under high pressure, the transition gas velocity from bubbly flow to churn-turbulent flow increases to about 10 - 12 cm/s. Under such conditions, when the flow is not well into the churn-turbulent flow regime, the proposed characterization methodology, to use gas holdup (and thereby an equivalent gas velocity U_{ge}) in determining the extent of liquid recirculation and turbulence in the column, does not hold. Therefore, estimating the effective axial dispersion coefficient on this basis grossly overpredicts the measured value. Considering for example, a gas velocity of 12 cm/s in a 15.8 cm diameter under a pressure of 15 atm, the present model predicts $D_{eff} = 505$ cm^2/s, while experimental measurements give $D_{eff} = 355$ cm^2/s (Wilkinson et al. 1993). Similar trends are seen for the experimental dispersion coefficients measured by Tarmy et al. in a 61 cm diameter column. In their case the maximum gas velocity considered was only 7 cm/s. Hence, the proposed analysis and methodology for evaluating the liquid axial dispersion coefficient in bubble columns operating under high pressure, can only be applied under conditions of high gas velocities when the system is well into the churn-turbulent flow regime, and does not hold for the transition flow regime.

6.3.3 Summary

A Taylor-type analysis of the two dimensional convection-diffusion equation has been performed which has resulted in an expression for the effective liquid dispersion coefficient in bubble columns, in terms of convective recirculation and turbulent diffusion. Using the scale-up equations for the mean liquid recirculation velocity and the average eddy diffusivities developed in Chapter 5, it is possible to evaluate the dispersion coefficient under various process conditions, in the churn-turbulent flow regime. Model predictions for the axial dispersion coefficient agree reasonably well with experimental data.